Atomically Thin, Half-van der Waals Metals enabled by Confinement Heteroepitaxy

Natalie Briggs[1,2,3†], Brian Bersch[1,2†], Yuanxi Wang[2,3†], Jue Jiang[4], Roland J. Koch[5,6], Nadire Nayir[3,7], Ke Wang[8], Marek Kolmer[9], Wonhee Ko[9], Ana De La Fuente Duran[1], Shruti Subramanian[1,2], Chengye Dong[1,2], Jeffrey Shallenberger[8], Mingming Fu[9], Qiang Zou[9], Ya-Wen Chuang[4], Zheng Gai[9], An-Ping Li[9], Aaron Bostwick[5], Chris Jozwiak[5], Cui-Zu Chang[4], Eli Rotenberg[5], Jun Zhu[4], Adri C. T. van Duin[1,3,7,8,10,11,12], Vincent Crespi[2,3,4,8], Joshua A. Robinson[1,2,3,8,13*]

[1]Department of Materials Science and Engineering, The Pennsylvania State University, University Park, PA 16802, United States of America
[2]Center for 2-Dimensional and Layered Materials, The Pennsylvania State University, University Park, PA 16802, United States of America
[3]2-Dimensional Crystal Consortium, The Pennsylvania State University, University Park, PA 16802, United States of America
[4]Department of Physics, The Pennsylvania State University, University Park, PA 16802, United States of America
[5]Advanced Light Source, Lawrence Berkeley National Laboratory, Berkeley, California 94720, United States of America
[6]The Molecular Foundry, Lawrence Berkeley National Laboratory, Berkeley, California 94720, United States of America
[7]Department of Mechanical Engineering, The Pennsylvania State University, University Park, PA 16802, United States of America
[8]Materials Research Institute, The Pennsylvania State University, University Park, PA 16802, United States of America
[9]Center for Nanophase Materials Sciences, Oak Ridge National Laboratory, Oak Ridge, TN 37831, United States of America
[10]Department of Chemistry, The Pennsylvania State University, University Park, PA 16802, United States of America
[11]Department of Engineering Science & Mechanics, The Pennsylvania State University, University Park, PA 16802, United States of America
[12]Department of Chemical Engineering, The Pennsylvania State University, University Park, PA 16802, United States of America
[13]Center for Atomically Thin Multifunctional Coatings, The Pennsylvania State University, University Park, PA 16802, United States of America
†Equally contributing authors
*Corresponding author
Email: jrobinson@psu.edu

Atomically thin two-dimensional (2D) metals may be key ingredients in next-generation quantum and optoelectronic devices. However, 2D metals must be stabilized against environmental degradation and integrated into heterostructure devices at the wafer scale. The high-energy interface between silicon carbide and epitaxial graphene provides an intriguing framework for stabilizing a diverse range of 2D metals. Here we demonstrate large-area, environmentally stable, epitaxial graphene/single-crystal 2D gallium, indium, and tin heterostructures. The 2D metals are covalently bonded to SiC below but present a non-bonded interface to graphene overlayer, i.e. they are "half van der Waals" metals with

strong internal gradients in bonding character. These non-centrosymmetric 2D metals open compelling opportunities for superconducting devices, topological phenomena, and advanced optoelectronic properties. For example, the reported 2D-Ga is a superconductor that combines six strongly coupled Ga-derived electron pockets with a large nearly-free-electron Fermi surface that closely approaches the Dirac points of the graphene overlayer.

Major advances in fundamental science have followed from the exfoliation, stacking, and encapsulation of atomically thin 2D layers[1]. The next step towards technological impact of 2D layers and heterostructures is to transition sophisticated "pick and place" devices to a *wafer-scale* platform. However, the sensitivity of 2D systems to interfacial reactions and environmental influences – especially for two-dimensional metals or small-gap semiconductors – poses challenges for large-scale integration. Very few metals resist degradation of their top few atomic layers upon environmental exposure, and for a 2D metal, these layers constitute the entire system. A general platform for producing *environmentally stable* and *wafer-scale* 2D metals that are not prone to interfacial interactions would represent a significant advance. Inspired by the success of wide-bandgap 2D gallium nitride[2], we turn focus onto the metal alone and demonstrate a platform dubbed **confinement heteroepitaxy** (CHet), where the interface between epitaxial graphene (EG) and silicon carbide (SiC) stabilizes crystalline 2D forms of Group-III (Ga, In) and group-IV (Sn) elements. Defect engineering of the graphene overlayer enables uniform, large-area intercalation at the high-energy SiC/EG interface; this interface then templates intercalant crystallization at a thermodynamically defined number of atomic layers. The unreactive nature of as-grown EG on SiC (graphene plus buffer layer) performs multiple services: (1) it only partially passivates the SiC surface underneath, thereby sustaining the high-energy interface that drives intercalation; (2) it lowers the energy of the (otherwise exposed) upper surface of the metal, thus facilitating 2D morphologies; (3) it protects the newly formed 2D metal from environmental degradation after intercalation through *in situ* healing of the graphene defects. Stability of these 2D metals in air over months greatly facilitates *ex situ* characterization and enables facile processing and device fabrication. Competing methods to obtain thin, single-crystal metal films are specific to certain metallic species (e.g. Au[3] or TiN[4]) and generally produce thicker, few-nm layers without *in situ* encapsulation, whereas CHet produces stable atomically-thin crystalline 2D forms of diverse metals which do not otherwise exist in nature.

Discussion

Unlike traditional EG intercalation methods[5–8], CHet (**Figure 1a**) uses plasma-treated EG and high-pressure (300 Torr) thermal evaporation to realize continuous films of crystalline 2D metals. Nominally monolayer EG is grown by silicon sublimation from 6H-SiC(0001)[9], after which exposure to an oxygen plasma generates defects in the EG layers. Metallic precursors such as Ga, Sn, and In situated in a crucible directly beneath EG are then heated with the EG/SiC to 700–800°C. The vaporized metal diffuses through EG defects to reach the EG/SiC interface. X-ray photoelectron spectroscopy (XPS) (**Figure 1b**) and Raman spectroscopy (**Figure 1c**) reveal how the EG defects evolve during CHet. O_2/He plasma treatments create defects in the EG that contain

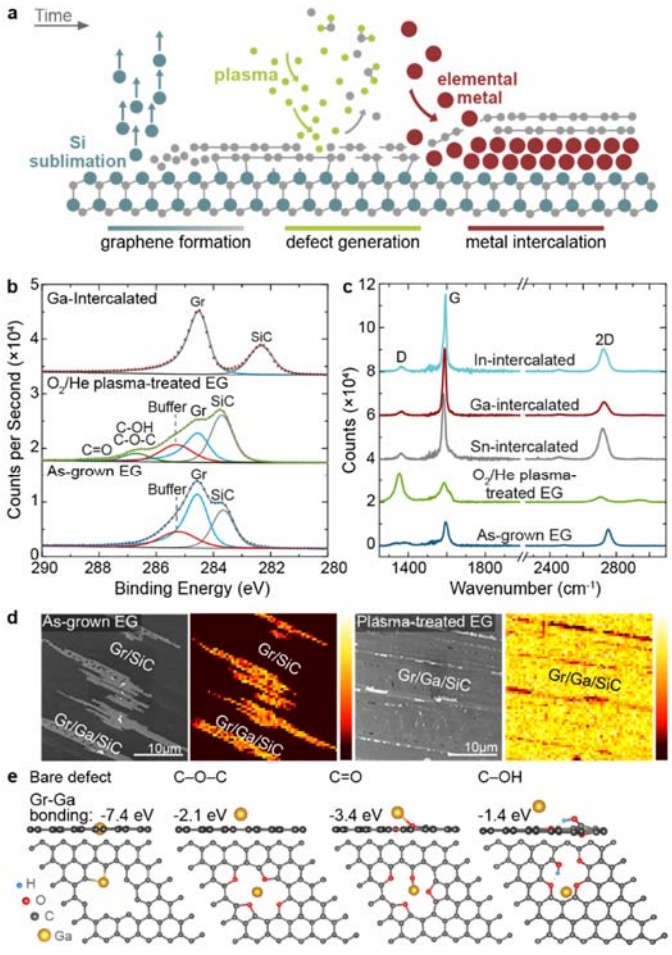

Figure 1: Confinement Heteroepitaxy with defect-engineered epitaxial graphene. (a) Schematic of CHet showing EG growth, O_2/He plasma treatment, and intercalation steps. (b) XPS showing C 1s for (bottom) as-grown EG, (middle) O_2/He plasma-treated EG, and (top) Ga-intercalated, O_2/He plasma-treated EG demonstrating the creation and annihilation of C–O bonds during CHet; this is confirmed by (c) Raman spectroscopy of as-grown EG, O_2/He plasma-treated EG, and metal-intercalated, O_2/He plasma-treated EG, where the defect peak (D peak) intensity is dramatically reduced as a result of the intercalation process. SiC Raman spectra are subtracted from the Raman data shown in (c). (d) SEM and accompanying Ga AES maps of Ga-intercalated, as-grown EG and Ga-intercalated, O_2/He plasma-treated EG. Defects formed due to plasma treatments lead to significantly improved intercalation uniformity, with >95% intercalant surface coverage when the EG is plasma treated. (e) DFT modelling of Ga atoms on optimized graphene sheets with bare, C−O−C, C=O, and C−OH passivated defects suggests that oxygen termination provides favorable energies for metal attraction and intercalation through the graphene sheet. The Ga binding energy to each defect is shown in each model.

C=O and C–OH and/or C–O–C bonds visible in the C 1s spectra (**Figure 1b**)[10,11]; these correlate with a 15× increase in the Raman D:G intensity ratio (I_D/I_G) (**Figure 1c**)[12]. Upon metal intercalation, signatures of carbon-oxygen bonding and the EG buffer layer peak disappear from the C 1s region (**Figure 1b**), and a metallic Ga 3d peak appears (**Figure S1**). Ultimately, metal intercalation (Ga, In, or Sn) releases the buffer layer[5–7] and removes carbon-oxygen bonding. XPS signatures remain stable even after >8 months in air (**Figure S2**). Intercalation also yields a pronounced (~5×) decrease in I_D relative to plasma-treated EG, and a 3–4× and 1–2× increase in I_G and I_{2D}, respectively, relative to as-grown EG (**Figure 1c**). The decreased I_D, lack of D′ and D+G modes, loss of carbon-oxygen bonding, and air stability of resulting 2D metals all suggest that the EG heals during intercalation at elevated temperatures[13–15] and subsequently acts as a barrier to oxidation post-synthesis. The strengthening of I_G and I_{2D} after intercalation may be attributed to metal/EG charge transfer and/or plasmon resonance[16–18]. Comparison of Auger electron spectroscopy (AES) (**Figures 1d, S3**) and Raman mapping (**Figure S4**) of EG/Ga samples prepared using pristine vs. plasma-treated EG reveals that plasma-treatments greatly increase the lateral coverage of intercalated Ga. Beyond a simple increase in intercalation sites, first-principles calculations indicate that Ga/EG bonding is strengthened with increasing vacancy size, where large, *unpassivated* defects bond covalently with Ga (**Figures 1e**, **S5**). First-principles calculations suggest that the termination of multivacancy graphene defects with oxygen moieties facilitates metal adhesion and transport to the underlying EG/SiC interface through intermediate metal binding energies that are weaker than those of unpassivated vacancies but stronger than those for hydroxyl terminations or the basal plane (**Figures 1e, S5**).

Two dimensional Ga, In, and Sn are 1–3 atomic layers thick and registered to the SiC substrate (**Figure 2a, c, e**). The dominant thickness observed can be explained by first-principles equilibrium phase stability calculations (**Figures 2b, d, f, S6**) that predict the layer number as a function of metal chemical potential. Based on first-principles calculations, the strong metal-SiC bonding stabilizes a 2D metal compared to the bulk 3D form, but this advantage is diluted by successive thickening of the intercalant so that the bulk phase is preferred beyond a certain thickness. These calculations predict a stability range of 1–3 layers for Ga, 1–2 layers for In, and 1 layer for Sn, all in encouragingly close agreement with scanning transmission electron microscopy (STEM) images (**Figure 2a, c, e**), which display 3 layers of Ga, 2 of In, and 1–2 of Sn (in the case of Sn, the blurring of the second Sn layer indicates a lower structural stability for this layer). This close correspondence suggests near-equilibrium growth conditions during CHet, i.e. a relatively high metal atom mobility, which is supported by the uniform metal coverage achieved. The high energy of the initial EG/SiC interface, which follows from the ineffectiveness of EG in terminating SiC dangling bonds, provides a strong thermodynamic driving force to 2D metal formation, suggesting a broader applicability of CHet to support additional species as 2D metals. The metal thicknesses shown in **Figure 2a, c, e** are uniform across the terraces of SiC, although some SiC terraces show uniform 2 layer Ga.

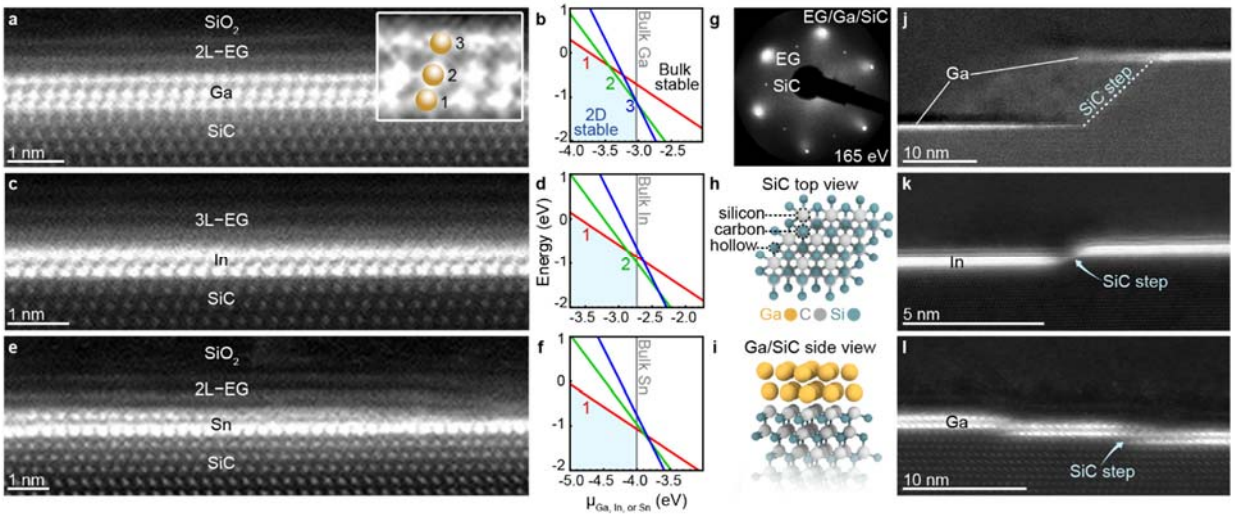

Figure 2: Atomic Structure of CHet-grown 2D metals. (a) Cross-sectional STEM showing 3 layers of Ga between EG and SiC. The inset shows different interlayer spacing of Ga layers. (b) Corresponding energy minimization calculations showing preferred Ga layer numbers. (c-f) Cross-sectional STEM and layer number calculations for In and Sn. Energy dispersive x-ray spectroscopy (**Figure S7**) confirms that intercalant layers match the respective precursor elements and are not oxidized. The grey, vertical lines in b, d, and f indicate the metal chemical potential of the bulk metal, and red, green, and blue lines indicate energy as a function of chemical potential for 1, 2, and 3 layers, respectively. The lowest line at a given potential indicates the ground state layer-number. (g) Acquired LEED pattern for EG/Ga/SiC indicating the presence of EG and SiC with no additional spots for a unique Ga (or In, Sn – **Figure S8**) structure, indicating the Ga is lattice matched to EG or SiC. (h) Top-down schematic of hexagonal SiC with silicon, carbon, and hollow sites labeled, where (i) intercalated Ga layers exhibit an ABC stacking over the SiC substrate. (j-l) Step bunching in the SiC surface can lead to discontinuities in the 2D metals, necessitating that SiC steps be few atoms in height to maintain structural and electrical continuity of 2D metal films.

An epitaxial relationship of the 2D metals to the SiC substrate is further supported by the observation in low-energy electron diffraction (LEED) of EG and SiC patterns, but no distinct spots corresponding to a structurally unique intercalant layer (**Figures 2g, S8**); i.e. the SiC diffraction pattern is shared by the metal. The 2.72 Å lateral Ga spacing observed via STEM also closely matches that of SiC (**Figure 2a, S9**). First-principles structural optimization provides

further insights into the epitaxial relationship of Ga to SiC (0001). Structural relaxations were performed for 1–3 layers of Ga initialized at sites projecting onto the silicon, carbon, and/or hollow sites of SiC (**Figures 2h, S10, S11, Table S1**). Adding a top bilayer graphene only affects band fillings without changing the relative stability of the Ga structures (**Table S1**), so it is not considered in these structural stability calculations. The ground-state locations for the first, second, and third layers of Ga are above the silicon (Ga_{Si}), carbon (Ga_{C}), and hollow (Ga_{hollow}) sites respectively (**Figure 2i**). This ABC stacking resembles a face-centered-cubic lattice cleaved along (111), matching the hexagonal arrangement of SiC (0001) and is possibly related to the metastable distorted FCC phase of Ga-III[19]. Ga registry weakens for increased metal thickness: the Ga_{Si} stacking site for single-layer Ga is 0.14 eV per unit cell (i.e. per 8.30 Å^2) more stable than Ga_{C} and Ga_{hollow}, but the ground states of Ga multilayers are preferred by only 0.05 eV against competing phases. Cross-sectional STEM (**Figure 2a**, **inset**) supports the calculated evolution with increasing thickness, where the interlayer spacing between the first and second Ga layers (2.19 Å) is significantly smaller than the second and third (2.36 Å). Density functional theory results show a pronounced shift from largely covalent bonding in the bottom Ga layer (templated against SiC) to comparably strong but more metallic bonding between the upper Ga layers and much weaker interaction between the upper Ga layer and the graphene overlayer (**Table S1**). Experimentally, epitaxy and metal continuity are interrupted by large steps in the SiC surface (**Figure 2j**), while smaller steps (**Figure 2k**) are less disruptive and single-atom steps (**Figure 2l**) are metal-continuous and appear to maintain epitaxy across the step.

The structural quality of 2D-Ga is reflected in the excellent agreement of ARPES measurements with calculations of the structurally optimized epitaxial system (**Figure 3a,** also **Figure S12** for 2D In). The high valence electron count of *p* block metals and the small lateral unit cell of epitaxial 2D-Ga yield an exceptionally large *s*-band Fermi velocity of 2×10^6 m/s, comparable to that of bulk Al and Ga (assuming a free electron model)[20] or In on Si(111)[21] and substantially larger than the band velocity of graphitic π states[22,23]. The calculated band structure (**Figure 3b**) shows color-coded projections of the total wavefunction onto the plane-wave components of the graphene (black) and Ga/SiC (blue) primitive cell, where bands are unfolded from the supercell Brillouin zone[24]. The most prominent features are three avoided crossings between *s* and *p* Ga bands, one along Γ-M_{Ga} and two along Γ-K_{Ga} (comparing to a freestanding frozen bilayer of Ga, **Figure S13**, the Ga *s*-band starts ~9 eV below the Fermi level). A large Ga-derived near-free-electron-like Fermi surface (**Figure 3c, d**) closely approaches the graphene Dirac points at K_{gr} and K'_{gr} with further electron pockets around the corners of the Ga Brillouin zone. The position of the graphene Dirac point 0.2–0.3 eV below the Fermi level (**Figure S14**) indicates that Ga (or In, **Figure S12**) electron dopes graphene by $8–10\times10^{12}$ cm^{-2}. This is supported by the Fermi surface of bilayer Ga/SiC calculated without graphene (**Figure 3e**) where the Fermi level is upshifted by 0.4 eV to be consistent with the measured ARPES band alignment (see **Figure S11**); this artificial upshift is not needed when using hybrid functionals, which generally yield more accurate band alignments (see SI for details on supercell strain imposed in calculations). Finally, the measured Fermi surface

clearly shows that the graphene Brillouin zone is rotated 30° from the underlying Ga/SiC zone; providing direct evidence for orientational epitaxy between Ga and SiC.

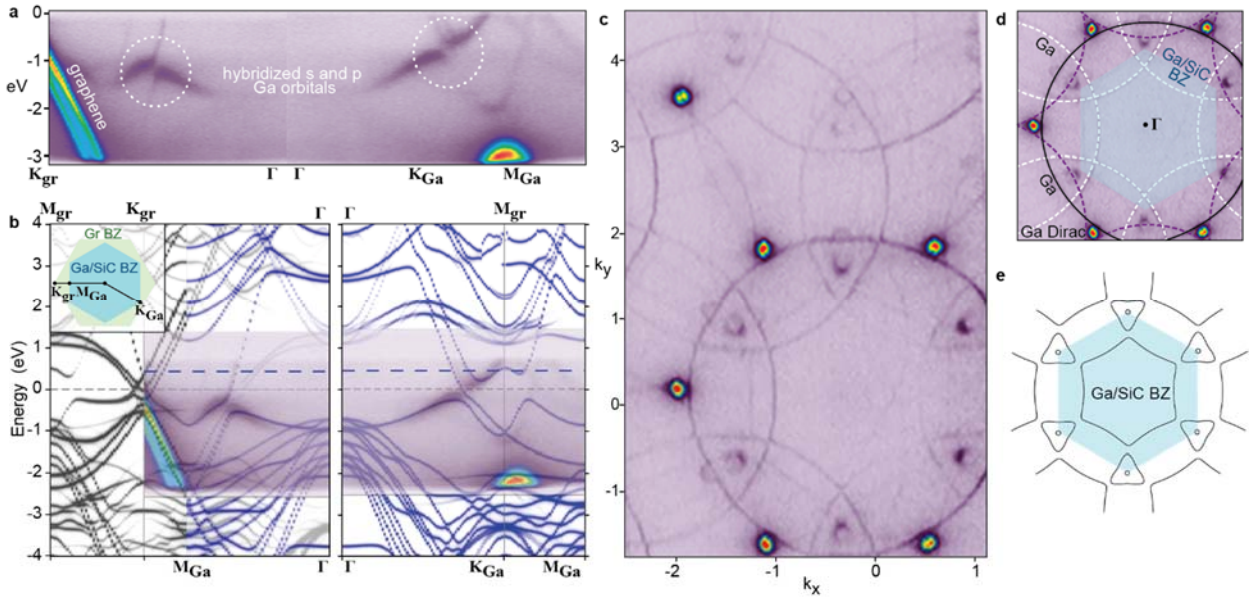

Figure 3: Electronic Structure of CHet-grown 2D Ga. (a) Measured ARPES spectra for EG/Ga/SiC showing EG and Ga bands near M_{Ga} and K_{Ga} and (b) Calculated band structure in black and blue overlaid with measured ARPES (purple). The effective unfolded band structures of 2×2 graphene + $\sqrt{3}\times\sqrt{3}$ R30º bilayer Ga/SiC along the Γ-M_{Ga} (Γ-K_{gr}) and the Γ-K_{Ga} (Γ-M_{gr}) directions are projected onto graphene (black) and Ga/SiC (blue), as indicated by the Brillouin zone paths in the inset (M_{gr} in the left panel and M_{Ga} on the right are from repeated zones). ARPES measurements along the same paths are superimposed. (c, d) ARPES-measured Fermi surface showing nearly-free-electron-like circular contours. Superimposed black, white, and purple circles in (d) correspond to nearly free electron like circular contours from Ga and are drawn to aid in comparison of experimental data with (e) DFT-calculated Fermi surface of bilayer Ga/SiC with the Fermi level shifted (to the blue dashed line in panel (b)) to match the measured band filling.

The air stability of 2D metals formed by CHet enables *ex situ* transport measurements without complex capping methodologies. A co-linear four-point-probe configuration with In dot contacts reveals a largely metallic behavior for 2D-Ga on small-step SiC from room temperature down to 4 K, below which a sharp 4-order-of-magnitude drop in resistance occurs (**Figure 4a**). Following definitions in Methods, T_c^{onset} = 3.95 K, and T_c^{zero} = 3.2 K, i.e. higher than in bulk orthorhombic α-Ga (1.08 K)[25], similar to that of metastable monoclinic□□-Ga (5.9–6.5K), and below that of metastable amorphous Ga (8.4 K)[26–28]. As expected, the transition drops and broadens with increasing perpendicular magnetic field $B_\perp$ (**Figure 4b**). R versus $B_\perp$ indicates B_c = 130 mT at 2 K with a corresponding coherence length $\xi_0 \sim 50$ nm (**Figure 4c**, **Methods**). A linear extrapolation of $B_c(T)$ from R(B) suggests a zero-Kelvin critical field $B_{c0} \approx 260$ mT and $\xi_0 \sim 36$ nm, higher than that of □-Ga ($B_{c0} \approx 6$ mT)[25] and β-Ga ($B_{c0} \approx 54$ mT)[28] (**Figure S15a**). Considering the very high Fermi velocity and moderate T_c, the system is likely not in the clean limit. Scanning tunneling microscopy/spectroscopy show quite uniform differential tunneling conductance (dI/dV) spectra at multiple locations on the sample (**Figure 4d, f, S15**). A superconducting gap with well-defined coherence peaks at ±0.6 meV is seen at 2.2 K (**Figure 4h**) and disappears at ~3 K, below the transport T_c (**Figure 4g**), perhaps due to a moderately reduced proximity-induced superconducting order parameter in the 2–3 layer EG overlayer[29]. The observation of a significant superconducting order parameter at the upper EG surface bodes well for the formation of superconducting heterostructures via proximity effect.

When crystallographic steps on SiC(0001) are less than 1 nm tall (**Figure 2k, l**), transport measurements that orient the current parallel or perpendicular to the steps have similar $T_c^{onset} \sim 4$ K and $T_c^{zero} \sim 3.2$ K (**Figure 4i**). Although steps more than 5 nm tall (**Figure 2j, 4j**) yield similar $T_c^{onset} \sim 3.8$ K for both directions, only parallel transport displays a fully developed superconducting transition with $T_c^{zero} \sim 2.5$ K, suggesting that transport perpendicular to large steps encounters a finite series resistance at the steps. Small-step 2D-Ga exhibits a Berezinskii-Kosterlitz-Thouless (BKT) transition temperature[30] of $T_{BKT} = 3.1$ K (2.9 K) for transport parallel (perpendicular) to the SiC steps (**Figure S17**), indicating a largely isotropic 2D superconducting transition in these samples. Note that I-V measurements up to the critical current (I_c) are limited by the experimental setup, and T_{BKT} is likely closer to 3.88 K (**Figure S17**) if extracted from curves closer to I_c. Full R(T) and R(B) curves for "large-step" 2D-Ga are provided in **Figure S18**. Epitaxial graphene synthesis must limit step bunching to ensure uniform superconducting films with isotropic transport. SiC step height and bunching can be mitigated by reducing the temperature of the pre-EG growth H_2 etch step[31], or through the delivery of carbon to the SiC

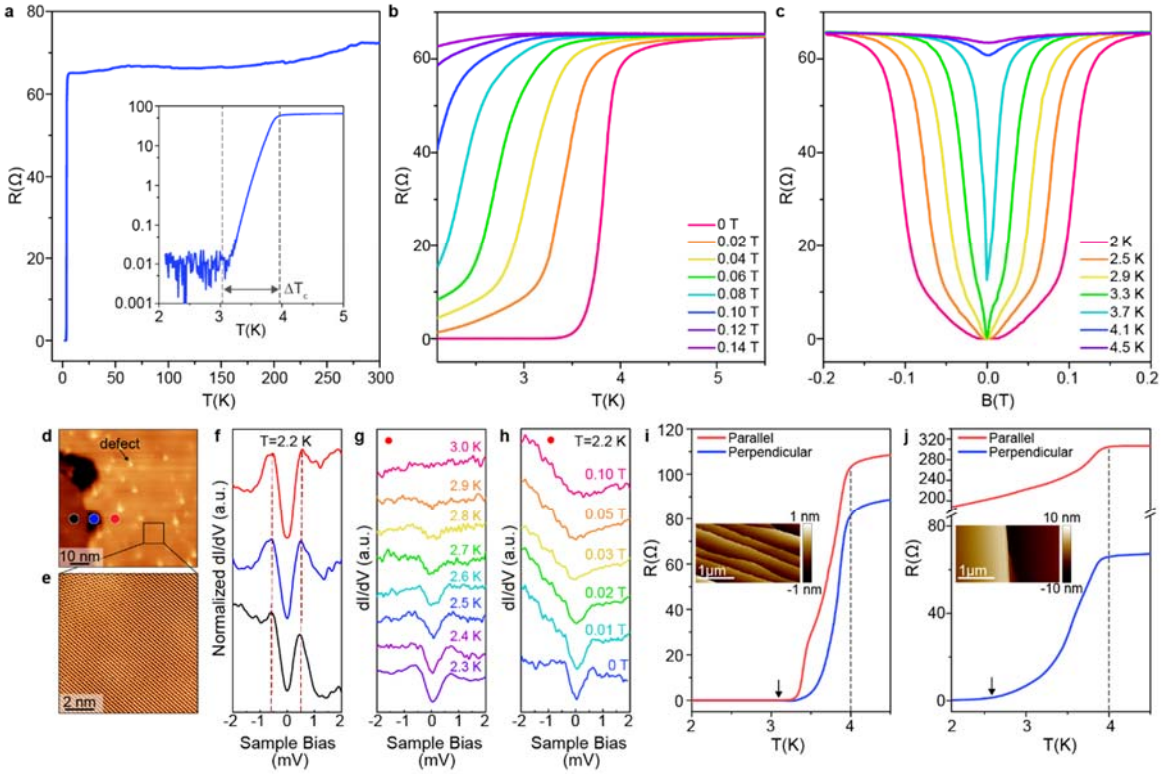

Figure 4: Superconductivity in 2D-Ga grown via CHet. (a) Zero-field R(T) curve for an optimized 2D-Ga (O_2/He plasma-treated EG, small-step, parallel configuration) film from 300 K to 2 K. Inset of (a): log-scale plot from 5 K to 2 K of the same curve. (b) R(T) curves showing a degradation in T_c and increase in residual resistance at 2 K with increasing out-of-plane magnetic field. (c) Resistance vs. out-of-plane magnetic field (R(B)) curves showing a similar degradation in the superconducting state with increasing temperature. The kink may be attributed to two superconducting phases, possibly from discrete 2 layer Ga and 3 layer Ga regions, step-edge interactions, or distinct superconducting transitions within a 3 layer Ga region. Data shown in (a-c) is from the same sample and measurement configuration. (d-e) Large-area and atomic resolution scanning tunneling microscopy images of the EG surface topography, respectively. (f) Differential conductance (dI/dV) spectra (normalized to 3.0 K spectra) taken at 2.2 K for the 3 different regions shown in (d). (g,h) Temperature-dependent (zero-field) and perpendicular magnetic-field-dependent (2.2 K) dI/dV spectra, respectively, of a region on the right-terrace in (d), marked by the red dot. (i,j) R(T) plots comparing perpendicular and parallel current directions performed on small-step and large-step samples (both using O_2/He plasma-treated EG), respectively. Black arrows indicate approximate T_c (zero) values, and dashed lines are meant to aid the eye (T = 4 K line). Insets: corresponding EG/SiC step edge morphology and height measured by AFM.

surface during EG growth to promote buffer layer nucleation and suppress mass transport across SiC that leads to step formation[32,33].

When considering the electronic origin of the superconductivity in 2D Ga/SiC, each of the constituent materials appears to be poor superconductors: SiC is semiconducting, EG is not as heavily doped (**Figure S14**) as in graphite intercalation compound superconductors, and 2D Ga exhibits nearly-free electron characters and thus would not lead to substantial T_c, since electron-lattice interactions are weak in nearly-free electron metals. We show using first-principles calculations that it is another Fermi surface manifold – small electron pockets around K – that mainly contributes to superconductivity. Using DFT, we calculate the electronic densities of states (DOS) near the Fermi level for α-Ga, β-Ga, and 1–3 layer 2D-Ga (**Figure 5a, b**) and also the Eliashberg spectral function $\alpha^2F(\omega)$ for 3 layer $Ga_{Si}Ga_CGa_C$ epitaxial to SiC without the graphene cap (**Methods, Figure S19**). α-Ga contains Ga dimers whose incipient covalency suppresses the density of states near the Fermi level, while □-Ga recovers a more nearly free-electron-like behavior (**Figure 5a**). 2 layer- and 3 layer-Ga/SiC (**Figure 5b**) exhibit a DOS at E_F similar to β-Ga. **Figure 5c** compares $\alpha^2F(\omega)$ and the cumulative electron-phonon coupling strength $\lambda(\omega)$ to the projected phonon density of states for the three individual Ga layers and the interfacial Si atom. The dominant contributions to the overall $\lambda = 1.62$ come from Ga vibrations below 120 cm^{-1}, with modest evidence near 180 cm^{-1} for distinct coupling channels specific to the (more covalent) lower layers of Ga and little sign of involvement from the interfacial Si. This is in contrast to previous reports attributing 2D superconductivity to interfacial bonding[34]. **Figure 5d** shows the momentum-resolved electron-phonon coupling[35] (□$_k$) across the Ga/SiC Brillouin zone for electronic states within ±0.5 eV of the Fermi energy; (**Figure S19** provides a similar plot for a narrower energy range). Dominant contributions to □$_k$ come from electron pockets near the two symmetry-inequivalent K points. Further decomposition of $\lambda_{k=K}$ by phonon wavevectors shows that the strongest contributions arise from intervalley scattering between the two K valleys (see discussion on **Figures S20 and S21**). Interestingly, this reciprocal-space structure to the coupling is similar to MoS_2, but here we have a p-block metal (with a large companion near-circular nearly-free-electron Fermi surface) with a small but crucial Fermi surface

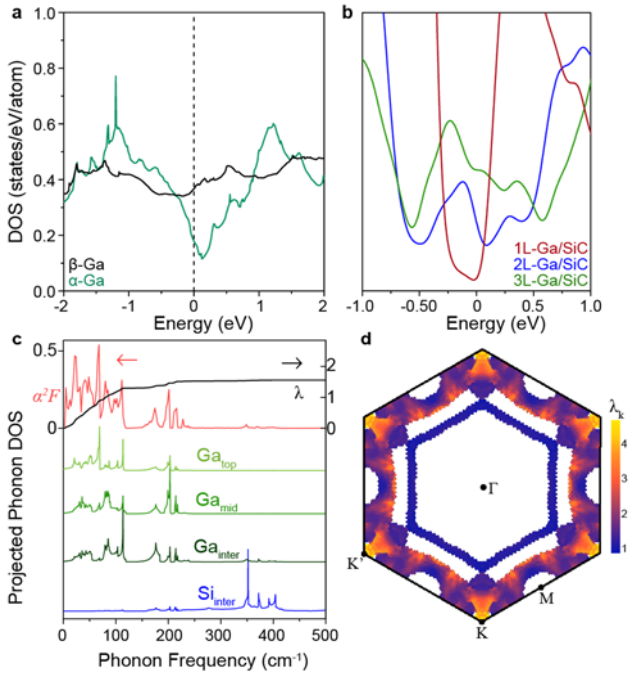

Figure 5: Theoretical calculations on graphene/2D-Ga heterostructures. (a) Electronic DOS vs. energy density functional theory (DFT) calculations for the two bulk phases of Ga including the stable α-Ga (low-T_c) and the metastable β-Ga (high-T_c) phases. (b) DOS vs. energy calculations for 1–3 layer Ga/SiC. (c) The Eliashberg spectral function $\alpha^2F(\omega)$ (red) compared with the projected phonon DOS of the three types of Ga atoms in 3 layer-Ga (shades of green) and the top Si atoms at the interface (blue). Importantly, the cumulative electron phonon coupling strength $\lambda(\omega)$ is superimposed in black at the top of (c). (d) Momentum-resolved electron-phonon coupling λ_k shows that the dominant contribution to coupling strength λ comes from the electron pockets near the K and K′ points in the Ga Brillouin zone. Graphene is not included in calculations.

manifold with a doped semiconductor character. A set of six pockets are indeed clearly seen in the ARPES measurement in **Figure 3c**, 30º rotated from the EG Dirac points; they correspond to hole pockets near K in **Figure 3b, e**, and are also similar in size to the pockets in the more accurate hybrid-functional-calculated bands of **Figure S11** (see discussions on **Figure S21** for details on the exact character of the pocket). The dominant contribution from these pockets is reassuring, since such strong coupling would not be expected from the more free-electron-like sheets of the Fermi surface. The Using the McMillian-Allen-Dynes formula[36,37] with $\lambda = 1.62$ and μ^* from 0.1 to 0.15 yields a T_c of 3.5 to 4.1 K, in good agreement with experiment. Literature reports of the electron-phonon coupling strength in β-Ga suggest that it is also a reasonably strong-coupled superconductor[38], unlike more weakly coupled α-Ga[36].

The large $\lambda = 1.62$ derived from the Ga states alone suggests that the EG layers are unlikely to be the driver of superconductivity in CHet-derived 2D-Ga. ARPES (**Figure 3**) provides further evidence towards this conclusion: the Fermi level is only 0.2–0.3 eV above the EG Dirac point, corresponding to $n \approx 8–10\times10^{12}$ cm^{-2}, which is 10–100× lower than superconducting Li-doped or Ca-intercalated EG[39,40]. In those cases, superconductivity is attributed to a partially filled band near the Γ point at a much higher level of charge transfer into EG than is observed in Ga-intercalated EG. Superconductivity in low-angle twisted bilayer graphene[41] likely exhibits a different origin from that in EG/Ga wherein the required interlayer twist is not present within the EG itself, although the environmental stability of 2D-Ga coupled with the controllable thickness of EG (1–3 layer post-intercalation) opens prospects to mechanically stack an additional (twisted) graphene monolayers onto EG/2D-Ga to create one of many hybrid superconducting systems possible based on the platform of highly stable CHet-derived 2D metals.

Conclusion

Confinement Heteroepitaxy (CHet) stabilizes 2D forms of 3D metals. The overlying graphene layers utilized in CHet not only help confine the 2D metals, but also serve as a seal to prevent oxidation of ultrathin non-noble metals, as revealed by the ability to perform extensive *ex situ* characterization of these materials. Whereas previously Au was arguably the only environmentally stable elemental metal, the realization of air-stable 2D heterostructures containing single-crystal, elemental metals and superconductors at the interface of EG and SiC opens the door to stabilizing diverse 2D allotropes of 3D metals and their alloys across the periodic table with potentially novel properties, all of which are candidates for incorporation into advanced multi-component heterostructures for next-generation quantum[42], photonic[43], and electronic applications.

Acknowledgements

Funding for this work was provided by the Northrop Grumman Mission Systems' University Research Program, Semiconductor Research Corporation Intel/Global Research Collaboration Fellowship Program, task 2741.001, NSF CAREER Awards 1453924 and 1847811, the Chinese Scholarship Council, an Alfred P. Sloan Research Fellowship, NSF DMR-1708972 and 1808900, and the 2D Crystal Consortium National Science Foundation (NSF) Materials Innovation Platform under cooperative agreement DMR-1539916. A portion of this research was conducted at the Center for Nanophase Materials Sciences, which is a DOE Office of Science User Facility, and at the Pennsylvania State University Materials Research Institute's Material Characterization

Laboratory. This research used resources of the Advanced Light Source, which is a DOE Office of Science User Facility under contract no. DE-AC02-05CH11231.

Contributions

N.B, B.B., Y.W., V.C., and J.A.R. wrote the paper with input from co-authors. N.B. performed confinement heteroepitaxy and XPS characterization, and assisted in Raman spectroscopy and SEM characterization. B.B performed Raman spectroscopy and SEM characterization and assisted in sample preparation and electrical characterization. Y.W. performed DFT modeling of graphene/Ga/SiC heterostructures in consultation with V.C. with input from J.Z., B.B., N.B., and J.A.R. J.J. performed electrical measurements under the direction of C.Z.C. with input from B.B and J.Z. R.K., A.B., and C.J. performed ARPES measurements under direction of E.R. N.N. performed graphene defect modeling under the direction of A.vD. K.W. performed cross-sectional STEM imaging. M.K. and W.K. prepared the LEED instrument for EG/metal/SiC samples and M.K. performed LEED measurements. A.D.L.F.D. assisted with confinement heteroepitaxy and material characterization. C.D. and S.S. performed the EG synthesis under the direction of J.A.R. J.S. assisted in XPS data analysis. M.F., Q.Z., G.Z., and A.P.L. performed scanning probe characterization. Y.W.C assisted with electrical measurements under the direction of J.Z. The authors would also like to acknowledge Haiying Wang for help with STEM sample cross-section preparation via FIB, Vince Bojan, Nabil Bassim, and Heshem Elsherif for help with Auger electron spectroscopy, and Max Wetherington for Raman spectroscopy support.

Data availability

The data that support the findings of this study are available at 10.6084/m9.figshare.c.4830711 or from the authors on reasonable request. See author contributions for specific data sets.

Code availability

Code used for computational investigations presented in this manuscript is available at gitlab.com/QEF/q-e/tree/qe-6.3 (EPW v5.0.0, Quantum Espresso v6.3) and www.vasp.at (Vienna Ab-initio Simulation Package).

Competing Interests

The authors declare no competing interests.

References

1. Rhodes, D., Chae, S. H., Ribeiro-Palau, R. & Hone, J. Disorder in van der Waals heterostructures of 2D materials. *Nat. Mater.* **18**, 541–549 (2019).
2. Al Balushi, Z. Y. *et al.* Two-dimensional gallium nitride realized via graphene encapsulation. *Nat. Mater.* **15**, 1166–1171 (2016).
3. Maniyara, R. A. *et al.* Tunable plasmons in ultrathin metal films. *Nat. Photonics* **13**, 328–333 (2019).
4. Shah, D., Reddy, H., Kinsey, N., Shalaev, V. M. & Boltasseva, A. Optical Properties of Plasmonic Ultrathin TiN Films. *Adv. Opt. Mater.* **5**, 1700065 (2017).
5. Riedl, C., Coletti, C. & Starke, U. Structural and electronic properties of epitaxial Graphene on SiC(0001): A review of growth, characterization, transfer doping and hydrogen intercalation. *J. Phys. D. Appl. Phys.* **43**, 374009 (2010).

6. Emtsev, K. V, Zakharov, A. A., Coletti, C., Forti, S. & Starke, U. Ambipolar doping in quasifree epitaxial graphene on SiC (0001) controlled by Ge intercalation. *Phys. Rev. B* **84**, 125423 (2011).
7. Gierz, I. *et al.* Electronic decoupling of an epitaxial graphene monolayer by gold intercalation. *Phys. Rev. B* **81**, 235408 (2010).
8. Virojanadara, C., Watcharinyanon, S., Zakharov, A. A. & Johansson, L. I. Epitaxial graphene on 6H-SiC and Li intercalation. *Phys. Rev* **82**, 205402 (2010).
9. Subramanian, S. *et al.* Properties of synthetic epitaxial graphene/molybdenum disulfide lateral heterostructures. *Carbon N. Y.* **125**, 551–556 (2017).
10. Moulder, J. F. & Chastain, J. *Handbook of x-ray photoelectron spectroscopy: a reference book of standard spectra for identification and interpretation of XPS data*. (Physical Electronics Division, Perkin-Elmer Corp, 1992).
11. Beamson, G. (Graham) & Briggs, D. (David). *High resolution XPS of organic polymers: the Scienta ESCA300 database*. (Wiley, 1992).
12. Eckmann, A. *et al.* Probing the Nature of Defects in Graphene by Raman Spectroscopy. *Nano Lett.* **12**, 3925–3930 (2012).
13. Vishwakarma, R. *et al.* Transfer free graphene growth on SiO_2 substrate at 250°C. *Sci. Rep.* **7**, 43756 (2017).
14. Araby, M. I. *et al.* Graphene formation at 150°C using indium as catalyst. *RSC Adv.* **7**, 47353–47356 (2017).
15. Fujita, J. *et al.* Near room temperature chemical vapor deposition of graphene with diluted methane and molten gallium catalyst. *Sci. Rep.* **7**, 12371 (2017).
16. Yi, C. *et al.* Evidence of Plasmonic Coupling in Gallium Nanoparticles/Graphene/SiC. *Small* **8**, 2721–2730 (2012).
17. Losurdo, M. *et al.* Demonstrating the Capability of the High-Performance Plasmonic Gallium-Graphene Couple. *ACS Nano* **8**, 3031–3041 (2014).
18. Khorasaninejad, M. *et al.* Highly Enhanced Raman Scattering of Graphene using Plasmonic Nano-Structure. *Sci. Rep.* **3**, 1–7 (2013).
19. Voloshina, E., Rosciszewski, K. & Paulus, B. First-principles study of the connection between structure and electronic properties of gallium. *Phys. Rev. B* **79**, 045113 (2009).
20. Ashcroft, N. W. & Mermin, N. D. *Solid state physics (p. 38)*. (Holt, Rinehart and Winston, 1976).
21. Yoshizawa, S., Kim, H., Hasegawa, Y. & Uchihashi, T. Disorder-induced suppression of superconductivity in the Si(111)-(7 × 3)-In surface: Scanning tunneling microscopy study. *Phys. Rev. B - Condens. Matter Mater. Phys.* **92**, 041410 (2015).
22. Yang, L., Deslippe, J., Park, C.-H., Cohen, M. L. & Louie, S. G. Excitonic Effects on the Optical Response of Graphene and Bilayer Graphene. *Phys. Rev. Lett.* **103**, 186802 (2009).
23. Zhang, Y., Tan, Y.-W., Stormer, H. L. & Kim, P. Experimental observation of the quantum Hall effect and Berry's phase in graphene. *Nature* **438**, 201–204 (2005).
24. Popescu, V. & Zunger, A. Extracting E versus $\vec{k}$ effective band structure from supercell calculations on alloys and impurities. *Phys. Rev. B* **85**, 085201 (2012).
25. Gregory, W. D., Sheahen, T. P. & Cochran, J. F. Superconducting Transition and Critical Field of Pure Gallium Single Crystals. *Phys. Rev.* **150**, 315–321 (1966).
26. Chen, T. T., Chen, J. T., Leslie, J. D. & Smith, H. J. T. Phonon Spectrum of Superconducting Amorphous Bismuth and Gallium by Electron Tunneling. *Phys. Rev.*

Lett. **22**, 526–530 (1969).
27. Wühl, H., Jackson, J. E. & Briscoe, C. V. Superconducting Tunneling in the Low-Temperature Phases of Gallium. *Phys. Rev. Lett.* **20**, 1496–1499 (1968).
28. Parr, H. & Feder, J. Superconductivity in β-Phase Gallium. *Phys. Rev. B* **7**, 166–181 (1973).
29. Werthamer, N. R. Theory of the Superconducting Transition Temperature and Energy Gap Function of Superposed Metal Films. *Phys. Rev.* **132**, 2440–2445 (1963).
30. Reyren, N. *et al.* Superconducting interfaces between insulating oxides. *Science* **317**, 1196–9 (2007).
31. M. H. Oliveira, Jr., T. Schumann, M. Ramsteiner, J. M. J. Lopes, and H. R. Influence of the silicon carbide surface morphology on the epitaxial graphene formation. *Appl. Phys. Lett.* **99**, 111901 (2011).
32. Kruskopf, M. *et al.* A morphology study on the epitaxial growth of graphene and its buffer layer. *Thin Solid Films* **659**, 7–15 (2018).
33. Kruskopf, M. *et al.* Comeback of epitaxial graphene for electronics: large-area growth of bilayer-free graphene on SiC. *2D Mater.* **3**, 041002 (2016).
34. Zhang, T. *et al.* Superconductivity in one-atomic-layer metal films grown on Si(111). *Nat. Phys.* **6**, 104–108 (2010).
35. Margine, E. R. & Giustino, F. Anisotropic Migdal-Eliashberg theory using Wannier functions. *Phys. Rev. B* **87**, 024505 (2013).
36. McMillan, W. L. Transition Temperature of Strong-Coupled Superconductors. *Phys. Rev.* **167**, 331–344 (1968).
37. Allen, P. B. & Dynes, R. C. Transition temperature of strong-coupled superconductors reanalyzed. *Phys. Rev. B* **12**, 905–922 (1975).
38. Garno, J. P. Simple high vacuum evaporation system with low-temperature substrate. *Rev. Sci. Instrum.* **49**, 1218–1220 (1978).
39. Ludbrook, B. M. *et al.* Evidence for superconductivity in Li-decorated monolayer graphene. *Proc. Natl. Acad. Sci. U. S. A.* **112**, 11795–9 (2015).
40. Ichinokura, S., Sugawara, K., Takayama, A., Takahashi, T. & Hasegawa, S. Superconducting Calcium-Intercalated Bilayer Graphene. *ACS Nano* **10**, 2761–2765 (2016).
41. Cao, Y. *et al.* Unconventional superconductivity in magic-angle graphene superlattices. *Nature* **556**, 43–50 (2018).
42. Fu, L. & Kane, C. L. Superconducting Proximity Effect and Majorana Fermions at the Surface of a Topological Insulator. *Phys. Rev. Lett.* **100**, 096407 (2008).
43. Boltasseva, A. & Shalaev, V. M. Transdimensional Photonics. *ACS Photonics* **6**, 1–3 (2019).

Methods

Epitaxial Graphene Synthesis and Plasma Treatment

Epitaxial graphene is synthesized via silicon sublimation from the (0001) plane of semi-insulating 6H-SiC (II-VI Inc.) at 1800°C, 700 Torr Argon, for 15 min (Ref.16, SI). EG layers were plasma treated using a Tepla M4L plasma etch tool, using 150 sccm O_2 and 50 sccm He under a pressure of 500 mTorr and power of 50 W for 60 seconds.

2D-Metal Intercalation

Metal intercalation was performed using an STF-1200 horizontal tube furnace fitted with a 1" outer diameter quartz tube. A custom-made alumina crucible from Robocasting Enterprises LLC. was used to hold 1×1cm EG/SiC substrates, which were placed with EG layers on the Si face of SiC facing downward, toward the inside of the crucible. 30–60 mg of metallic Ga (Sigma Aldrich, 99.999%), In powder (Alfa Aesar, -325 mesh, 99.99%), or Sn granules (Alfa Aesar, 99.5%) were placed in the crucible directly beneath the EG/SiC substrate. The crucible with EG/SiC and the respective metal precursor was then loaded into the tube furnace and evacuated to ~5 mTorr. The tube was then pressurized to 300–700 Torr with Ar. At this time, the furnace was heated to 700–800°C under a ramp rate of 20°/minute and Ar flow of 50 sccm. The furnace was held at the growth temperature for 30 minutes, then cooled to room temperature.

X-ray photoelectron spectroscopy

X-ray photoelectron spectroscopy measurements were carried out with a Physical Electronics Versa Probe II equipped with a monochromatic Al K_α X-ray source ($h\nu$=1486.7 eV) and a concentric hemispherical analyzer. High resolution spectra were obtained over an analysis area of 200 μm at a pass energy of 29.35 eV for C 1s, Si 2p, Ga 3d, and Ga 2p regions. O 1s regions were collected with a pass energy of 46.95 eV. The acquired spectra were fitted Lorentzian line shapes, and the asymmetric graphene peak fit was derived from exfoliated highly oriented pyrolytic graphite and H-intercalated EG reference samples. Spectra were charge referenced to this graphene peak in C 1s corresponding to 284.5 eV. A U 2 Tougaard background was used to fit XPS spectra.

Raman spectroscopy

Raman Spectroscopy is performed with a Horiba LabRam Raman system using a wavelength of 488nm and a power of 4.6 mW. Spectra are acquired with an integration time of 30s, using a 600 grooves/mm grating.

Cross-sectional transmission electron microscopy

Cross-sectional samples for STEM imaging were prepared by *in situ* lift-out via milling in a FEI Helios NanoLab DualBeam 660 focused ion beam (FIB). Prior to FIB, ~40/5/10 nm of SiO_2/Ti/Au was deposited via electron-beam evaporation in a Kurt J. Lesker Lab18 evaporator, to improve contrast during STEM imaging at low magnifications. Cross-sections were prepared using a Ga^+ ion beam at 30 kV then stepped down to 1 kV to avoid ion beam damage to the sample surface.

High resolution scanning transmission electron microscopy (STEM) of sample cross sections was performed in a FEI dual aberration corrected Titan3 G2 60-300 S/TEM at 200kV using a high angle annular dark field (HAADF) detector. The HAADF detector (Fischione) has a collection angle of 51–300 mrad for Z-contrast imaging. A beam current of 70pA, beam convergence of 30 mrad (C2 aperture of 70 μm), and camera length of 115 mm are used for STEM image acquisition. The STEM EDS maps are collected by using the superX EDS system, which has 4 EDS detectors surrounding the sample.

Low-energy electron diffraction

Low-energy electron diffraction measurements of EG/Ga/SiC, EG/In/SiC, and EG/Sn/SiC samples were performed using LEED Spectrometer BDL800IR-MCP manufactured by OCI Vacuum Microengineering. Samples were first degassed at 200°C for 30 minutes under UHV to desorb surface moisture and contaminants. LEED patterns were then acquired at room temperature using constant primary beam currents of 10 nA and beam energies of 50 eV–250 eV, in 1 eV steps.

Angle-resolved photoemission spectroscopy

Angle-resolved photoemission spectroscopy measurements were performed at the Microscopic and electronic structure observatory (MAESTRO) beamline at the Advanced Light Source at Lawrence Berkeley National Lab. The sample was annealed at 550 K for 30 minutes in the end-station before measurements to remove adsorbates from the transfer of the sample through air. Measurements of EG/Ga/SiC and Gr/In/SiC structures were performed using a photon energy of 140 eV and 110 eV, respectively. Photoemission spectra were collected by moving the sample around one angle while using the angle resolved mode of a Scienta R4000 electron analyzer for the collection of the other angular axis.

Transport measurements and T_c, B_c, and T_{BKT} extraction:

Transport measurements were carried out in a Quantum Design physical property measurement system (PPMS) system. Contacts were made to the EG/Ga heterostructure by lightly scratching the film surface with a diamond scribe or tweezers, and then lightly pressing or soldering In dots onto the scratched region. This was done in a casual attempt to make side-contact to the 2D-Ga. In dots were arrayed in a standard co-linear four-point-probe configuration with contact pitch on the order of hundreds of microns. All resistance measurements were made with an excitation current of 1 μA. T_c(onset) is defined as the intersection of linear extrapolations of the transition and normal regions. The linear fit for the transition region is the region of maximum slope, which is consistent for the entire transition width as seen in the log plot inset in **Figure 4a**. $T_c(0.5R_N)$ is defined as the temperature at which the sample reaches half of its normal resistance. T_c(zero) is defined as the temperature at which resistance effectively reaches a zero-resistance state i.e. the noise floor of the PPMS system ~ 0.01 Ω. The transition width ΔT_c is defined as the change in temperature between the T_c(onset) and T_c(zero). Various T_c values are provided in order to help comparison with other works in literature which may use different values. Critical field $B_{c2}(0.9R_N)$ is defined as the magnetic field at which the sample reaches 90% of its normal resistance. Coherence length is estimated from $B_{c2}(T) = \frac{\Phi}{2\pi\xi_0^2}$.

Scanning tunneling spectroscopy/microscopy (STS/STM):

Ga-intercalated EG/SiC was studied using ultra-high vacuum low-temperature scanning tunneling microscope with *in situ* out of plane magnetic field at the Center for Nanophase Materials Sciences at Oak Ridge National Laboratory. The sample was preheated to 200°C to remove surface adsorbates at UHV with a base pressure of 2×10^{-10} Torr before transferring *in situ* to STM stage. STM/S was conducted using mechanically cut Pt-Ir tip. All Pt-Ir tips were conditioned and checked using clean Au (111) surface before each measurement. Topographic images were acquired in constant current mode with the bias voltage applied to the samples. All the spectroscopies were obtained using the lock-in technique with bias modulation at 973 Hz. The STM image in **Figure 4d** was taken at V_b = 10 mV and I_t = 400 pA. The STM image in **Figure 4e** was taken at V_b = -100 mV, I_t = 100 pA. The dI/dV spectra in **Figures 4f-h** were measured at V_b = 5 mV, I_t = 400 pA, and ΔV = 0.1 mV.

Theory

i. Graphene defect generation/passivation and Ga adsorption: All density functional theory calculations investigating the role of plasma treatment on graphene defects and Ga intercalation were performed in Quantum Espresso (SI ref. 17), using projected augmented wave (PAW) pseudopotentials (SI ref. 18, 19) and the Perdew-Burke-Ernzerhof parametrization of the generalized gradient approximation exchange-correlation functional (GGA-PBE, SI ref. 20, 21). A 5×5×1 Γ-centered k-point mesh was applied for Brillouin zone integration. Planewave expansions were truncated at an energy cut-off of 408 eV for wavefunctions and at 4080 eV for charge densities. The Marzari-Vanderbilt cold smearing scheme (SI ref. 22) was applied with a broadening of 0.1 eV. Structural relaxations used the Broyden–Fletcher–Goldfarb–Shanno algorithm with a force threshold of 0.025 eV/Å. A vacuum layer of 20 Å was inserted in the direction normal to the graphene sheets to minimize the spurious interactions across the periodic boundary. The models in the figures were visualized using OVITO (SI ref. 23) and VESTA (SI ref. 24) software.

ii. 2D Ga phase stability and electronic structure calculations: All density functional theory calculations on phase stabilities and electronic structure were performed using the GGA-PBE exchange-correlation functional (SI ref. 20, 21) and the PAW pseudopotentials (SI ref. 18,19). Plane-wave expansions were truncated at an energy cutoff of 500 eV. All structural relaxations were performed using dipole corrections to the total energy (SI ref. 25) and to the electrostatic potential (SI ref. 26) in the out-of-plane direction, until the remaining forces are within 0.01 eV/Å. Brillouin zone samplings are performed on grids with k-point densities equivalent to that of a 20×20×1 grid for a 1×1 Ga/SiC unit cell. All Ga/SiC calculations were performed using 7 repeating units of SiC along the *z* direction as substrate, capped by Ga from above and by hydrogen from below. Graphene/Ga/SiC calculations were performed using 5 repeating units along the *z* direction for the a 2×2 graphene + √3×√3 R30º Ga/SiC supercell, and 3 repeating units for the a 5×5 graphene + 4×4 R0º Ga/SiC supercell to alleviate the computational demand of accommodating more atoms in the large supercells. Band unfolding were performed using the GPAW package (SI ref. 27); all other calculations were performed by the Vienna Ab Initio Package (VASP) (SI ref. 28). Fermi surfaces of Ga/SiC are calculated on a 40×40×1 grid and interpolated onto a 200×200×1 grid for plotting. Band structures at the hybrid functional level were calculated using the range-separated form of Heyd, Scuseria, and Ernzerhof (SI ref. 29) (HSE06, i.e. with a range-separation parameter of 0.2 $Å^{-1}$) and using structures relaxed at the PBE level. Self-consistent HSE06 calculations were performed on a 12×12×1 k-point grid. For the DOS of bilayer Ga in **Figure 5b**, we artificially shift E_F by 0.5 eV to account for the additional (undetermined) electron doping so the band alignment agrees with ARPES measurements. As for the DOS calculations carried out on hexagonal 2 layer and 3 layer-Ga/SiC, the $Ga_{Si}Ga_C$ and $Ga_{Si}Ga_CGa_C$ stacking sequences were used, respectively. The $Ga_{Si}Ga_CGa_C$ stacking sequence occupies one of the lower energy configurations out of all the possible stacking sequences for 3 layer-Ga and most closely matches the band structure as directly measured in ARPES (**Figures S10-11, Table S1**. Thus, $Ga_{Si}Ga_C$ and $Ga_{Si}Ga_CGa_C$ stackings were used to calculate the DOS and the $Ga_{Si}Ga_CGa_C$ stacking was used to calculate T_c (**Figure S19a**).

iii. Electron-phonon interactions: All calculations related to electron-phonon interactions are performed in a cell with only two SiC units, due to the heavy computational demand of these routines; SiC slabs are passivated from below by H atoms with the same mass as Si. The starting-point electronic charge density is calculated on a 12×12×1 Γ-centered k-point grid.

Electronic wavefunctions are then computed for a 6×6×1 grid. The phonon dispersion is calculated using density functional perturbation theory based on the same 6×6×1 grid. All computations above are performed by the Quantum ESPRESSO package using the local density approximation exchange-correlation functional, Hartwigsen-Goedeker-Hutter norm-conserving pseudopotentials, and a plane wave expansion cutoff of 1090 eV. To achieve a dense sampling of electron-phonon coupling matrix elements across the Fermi surface, we construct electronic and phonon Wannier functions based on wavefunctions and phonon modes sampled on the coarse 6×6×1 grid and generate interpolations onto a 96×96×1 grid, as implemented by the EPW code. Wannier functions are initialized by projecting the following orbitals onto Bloch wavefunctions: two *s* and one p_z for each Ga, one sp^3 orbital for each Si, and one sp^3 for each C. An outer disentanglement window (i.e. one that captures all targeted bands with the chosen orbital characters) coincides with the entire energy range (**Figure S19b**). An inner window (where all Bloch states are included within the projection manifold) spans the energy range from the lower bound of **Figure 19b** up to 1 eV above the Fermi level. See SI for more details on equations and references used.

Supplemental Information

Atomically Thin, Half-van der Waals Metals enabled by Confinement Heteroepitaxy

Natalie Briggs[1,2,3†], Brian Bersch[1,2†], Yuanxi Wang[2,3†], Jue Jiang[4], Roland J. Koch[5,6], Nadire Nayir[3,7], Ke Wang[8], Marek Kolmer[9], Wonhee Ko[9], Ana De La Fuente Duran[1], Shruti Subramanian[1,2], Chengye Dong[1,2], Jeffrey Shallenberger[8], Mingming Fu[9], Qiang Zou[9], Ya-Wen Chuang[4], Zheng Gai[9], An-Ping Li[9], Aaron Bostwick[5], Chris Jozwiak[5], Cui-Zu Chang[4], Eli Rotenberg[5], Jun Zhu[4], Adri C. T. van Duin[1,3,7,8,10,11,12], Vincent Crespi[2,3,4,8], Joshua A. Robinson[1,2,3,8,13*]

[1]Department of Materials Science and Engineering, The Pennsylvania State University, University Park, PA 16802, United States of America
[2]Center for 2-Dimensional and Layered Materials, The Pennsylvania State University, University Park, PA 16802, United States of America
[3]2-Dimensional Crystal Consortium, The Pennsylvania State University, University Park, PA 16802, United States of America
[4]Department of Physics, The Pennsylvania State University, University Park, PA 16802, United States of America

[5]Advanced Light Source, Lawrence Berkeley National Laboratory, Berkeley, California 94720, United States of America
[6]The Molecular Foundry, Lawrence Berkeley National Laboratory, Berkeley, California 94720, United States of America
[7]Department of Mechanical Engineering, The Pennsylvania State University, University Park, PA 16802, United States of America
[8]Materials Research Institute, The Pennsylvania State University, University Park, PA 16802, United States of America
[9]Center for Nanophase Materials Sciences, Oak Ridge National Laboratory, Oak Ridge, TN 37831, United States of America
[10]Department of Chemistry, The Pennsylvania State University, University Park, PA 16802, United States of America
[11]Department of Engineering Science & Mechanics, The Pennsylvania State University, University Park, PA 16802, United States of America
[12]Department of Chemical Engineering, The Pennsylvania State University, University Park, PA 16802, United States of America
[13]Center for Atomically Thin Multifunctional Coatings, The Pennsylvania State University, University Park, PA 16802, United States of America
†Equally contributing authors
*Corresponding author
Email: jrobinson@psu.edu

Technological Motivation and Impact of CHet and 2D Metals

EG/SiC intercalation studies reveal that material interfaces serve as an unexplored realm for creating and stabilizing never-before-seen 2D materials. The findings presented in this manuscript lay a foundation for interface engineering as a route to stabilizing 2D layers, thus expanding the library of 2D material synthesis techniques beyond exfoliation and direct growth. The impacts of intercalated, 2D metals extend to high-quality quantum heterostructures, new sensor platforms, and exceptional nonlinear optical responses.

Furthermore, crystalline 2D and interfacial superconductors are of great interest to the scientific community due to potential for unconventional properties that may lead to new physics. This manuscript focuses on superconducting 2D Ga, but the underlying process of stabilizing 2D superconductors (Nb, Pb, etc.) can be applied broadly. The work presented in this manuscript serves as the first joint experiment/theory analysis that elucidates the microscopic mechanism of superconductivity in a prototypical atomically-thin metal. We demonstrate BCS-type superconductivity in the semiconductor-supported 2D metal system, a platform that allows straightforward analysis of dimensionality effects, avoiding complexities such as strong electron correlations in other platforms supporting 2D superconductivity (e.g. FeSe/STO or cuprate interfaces). Prior to the current study, the main challenge of this type of platform (2D

metal/semiconductor) is the limitation to techniques utilizing ultra-high vacuum environments such as MBE[1], since 2D superconductivity is generally fragile against disorder; in fact no simple (i.e. not involving strong electron correlation) superconductor system studied to date is free from the requirement of UHV conditions[2]. The extension of confinement heteroepitaxy (CHet) to heavy elements such as Sn also enables future research on exotic pairing mechanisms in 2D superconductors, as demonstrated in a recent report based on 2D-Sn under prepared under UHV[3], where a new type of Ising pairing allows superconductivity to survive under in-plane magnetic fields at 2-4 times the Pauli limit.

Finally, within BCS-type simple 2D superconductors, previous experimental reports, e.g. on 2D Pb on Si[1], did not provide direct explanation of the microscopic mechanism contributing to superconductivity, giving only indirect evidence that the metal-substrate interface increases electron-phonon coupling λ from <0.9 (thick Pb films) to ~1. Follow-up first-principles theory work[4] only estimated macroscopic quantities such as λ and T_c, without further microscopic analysis to differentiate the interfacial electronic and phononic contributions to λ from the bulk metal or substrate contributions. At a more fundamental level, the conventional wisdom is that nearly free electron metals (evidenced by the Fermi circles in ARPES for 2D Ga and the free-electron-like bands[1,5]) are either not superconducting at all or very poor superconductors, since the electron-lattice interaction in a nearly-free electron system is weak. This manuscript shows how 2D Ga can still be superconducting despite exhibiting free-electron character using a microscopic analysis of first-principles results and ARPES data.

Experimental & Computational Supporting Data

X-ray photoelectron spectroscopy

Figure S1 shows XPS spectra for C, Si, O, Ga, Sn, and In for different intercalated samples. Panels (a-c) show spectra acquired from a standard EG/Ga/SiC sample, where EG is exposed to an O_2/He plasma prior to intercalation. Ga is then intercalated at standard conditions of 800°C and 300 Torr. Intercalation leads to a shift in the C 1s peak for SiC and the Si 2p peak by 1.4-1.5 eV. A small peak near 283.5 eV may be fitted to the C 1s spectrum in S1(a), and is believed to correspond to a fraction of C in the EG buffer layer that remains bonded to SiC following the intercalation procedure. Ga-intercalated samples exhibit metallic Ga 3d peaks (S1(c)) and two higher binding energy peaks in the Ga 3d region which could correspond to Ga_2O_3 (at 21 eV), and GaO_x or Ga-Si (at 19.3 eV), indicating that some Ga remains on the surface of the EG and subsequently oxidizes following exposure to ambient. Figure S1(d-f) correspond to a Ga-intercalated sample in which EG was not exposed to an O_2/He plasma prior to Ga intercalation. As a result, Ga intercalation does not occur uniformly across all EG/SiC terraces. Thus, the sample is referred to as partially-intercalated, and contains island-like regions of intercalated Ga. As a result of inhomogeneous Ga intercalation, the 200μm acquisition area reflects a mixture of EG still containing a buffer layer that is bonded to SiC, as well as EG that is decoupled from SiC via intercalated Ga. The C 1s SiC peak in S1(d) at 283.6 eV is hypothesized to correspond to the former case, and the C 1s SiC peak at 282.2 eV to the latter. This heterogeneous surface is also reflected in the Si 2p region in S1(e), where two sets of Si 2p peaks are observed (one at 101.3 eV and 101.9 eV, and one at 99.8 eV and 100.5 eV). The Ga 3d region collected from this sample shows peaks similar to those in S1(c), however, the higher binding energy peaks at 19.2 eV and 20.9 eV are more intense relative to metallic Ga 3d peaks than those in S1(c). C 1s and Si 2p spectra are also shown for a reference H-intercalated EG sample (in which EG is not exposed to an O_2/He plasma prior to intercalation). H intercalation also results in a shift in the SiC C 1s and Si 2p peaks by ~1 eV. Because the spectra are charge referenced to the sp^2 C (Gr) peak at 284.5 eV, relative changes in the Gr peak position are not investigated. O 1s spectra are shown for reference. Fully Ga-intercalated samples show greatest O 1s intensity. This could be due to regions of oxidized Ga that are not intercalated, but rather are deposited on the surface of EG, as shown in Figure S3.

XPS spectra are also shown for In- and Sn-intercalated samples prepared at 700°C and 300 Torr using O_2/He plasma-treated EG. The characteristic C 1s line shape of intercalated-EG is observed for both In and Sn-intercalated samples. The presence of intercalated In and Sn is further confirmed through cross-sectional STEM (main text Figure 2).

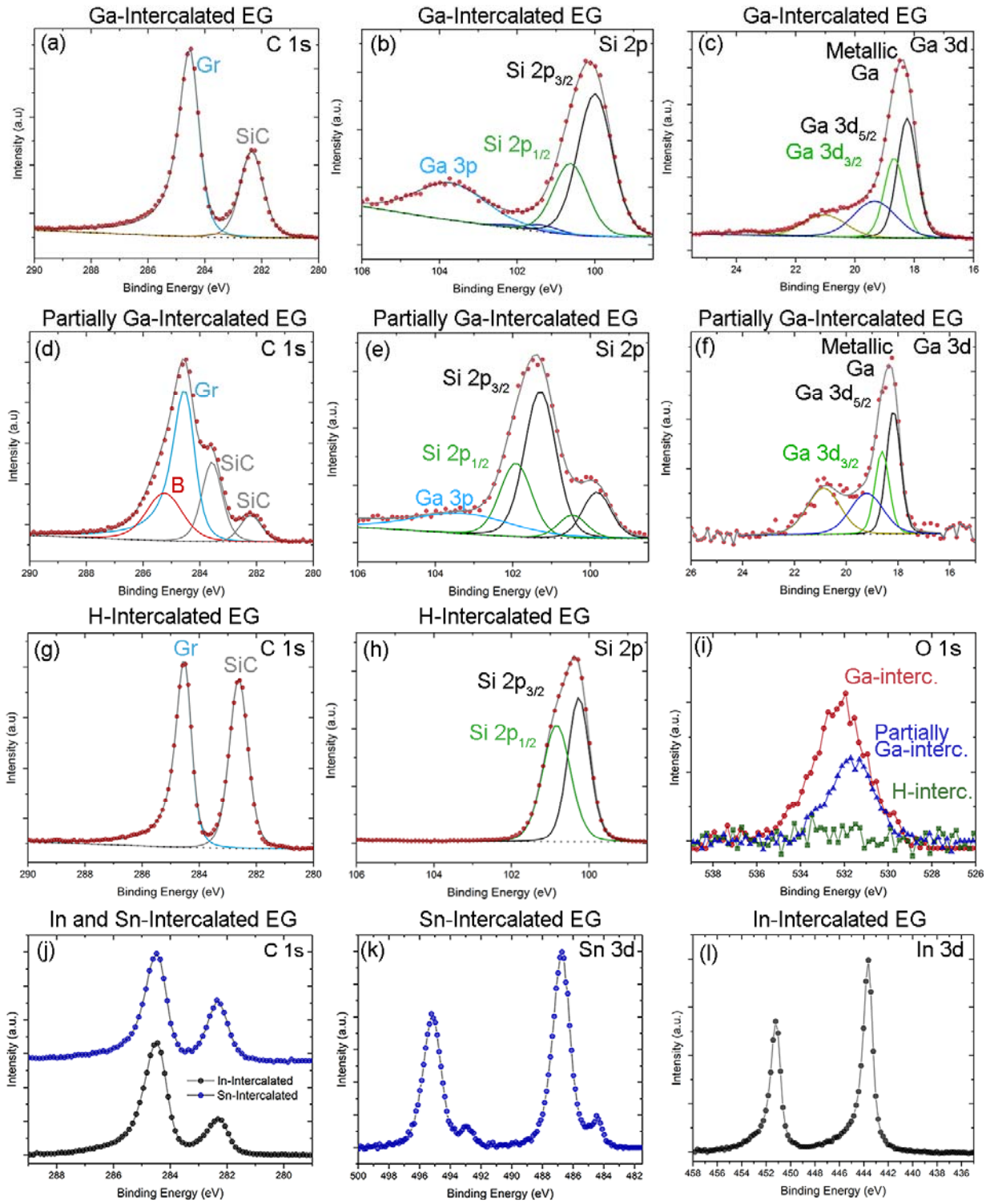

Figure S1: X-ray photoelectron spectroscopy spectra for Ga-intercalated samples where EG is O_2/He plasma-treated prior to intercalation (a-c) and where EG is not O_2/He plasma-treated prior to intercalation (d-f). (g, h) Show H-intercalated samples where EG is not O_2/He plasma-treated prior to intercalation. H-intercalated samples serve as a standard reference. The C 1s line shape used to fit the EG Gr peak is derived from the C 1s spectrum in (g). (i) O 1s for intercalated samples, where the maximum O 1s signal detected in (i) is corresponds to approximately ~2000 counts. (j-l) Show C1s, Sn 3d, and In 3d spectra for intercalated In and Sn samples (using O_2/He plasma-treated EG).

Gallium-intercalated samples are stable in air for over 8-months, as measured by XPS. Little difference in C 1s, O 1s, Ga 3d, and Si 2p peaks is detected between freshly-prepared and 8-month-old 2D Ga samples. The stability of metal, carbon, and oxygen signals over time is evidence of epitaxial graphene layer healing during the intercalation process.

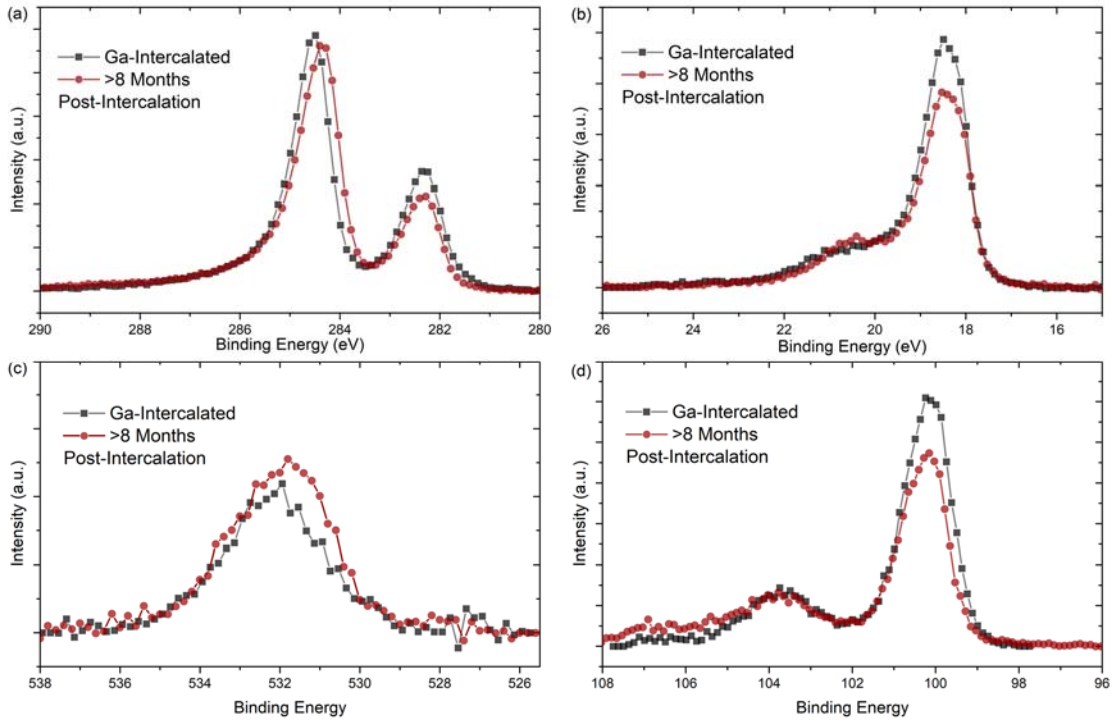

Figure S2: Stability of EG/Ga sample 8 months and 21 days post synthesis. (a-d) XPS characterization of a Ga-intercalated sample post-synthesis (within several days) and >8 months later. C 1s, Ga 3d, O 1s, and Si 2p high resolution spectra show little change following exposure of the sample to ambient. Two different samples were used for XPS characterization, so some differences in spectra may be attributed to sample-to-sample variation. The 8-month old sample was routinely left out in air for days and weeks at a time. Importantly, O 1s intensity is relatively unchanged after >8 months.

Auger electron spectroscopy

Auger maps of 2D-Ga and In samples synthesized using O_2/He plasma-treated EG are consistent with other characterization methods (XPS, STEM), where strong C and Ga/In signals are observed across a 10×10μm mapped area. AES maps were acquired for EG/SiC samples which can contain a range of different step-edge heights. The diagonal lines in Figure S3(b-e, g-j) correspond to steps in the SiC which can contain additional EG layers. The increased C signal at the large diagonal features in Figure S3(c) and (h) is consistent with a greater number of EG layers, and is accompanied by reduced Ga and In signal Figure S3(b, g), which is likely due to signal attenuation from a greater number of overlying EG layers.

Many prior intercalation works utilize UHV conditions and a two-step intercalation process in which metal is evaporated onto the EG surface and the sample is then heated to achieve metal intercalation. This process can leave significant amounts of residual metal on the EG surface. Unlike these two-step UHV approaches, CHet employs heating of the EG/SiC substrate during metal evaporation. This limits adsorption of metal onto the EG surface during intercalation. Figure S3(a) and (f) demonstrate the typical metal particle density on the EG as a result of the CHet process. These metal particles are typically ~100–500 nm in diameter and do not impact superconductivity measurements. Follow-up studies of precursor mass, intercalation pressure, and precursor build-up within the CHet crucible may enable further reduction of metal particle deposition on the EG surfaces. Regions of the intercalated samples showing increased oxygen signal (Figure S3(e) and (j)) can be attributed in part to small metal-oxide islands that have

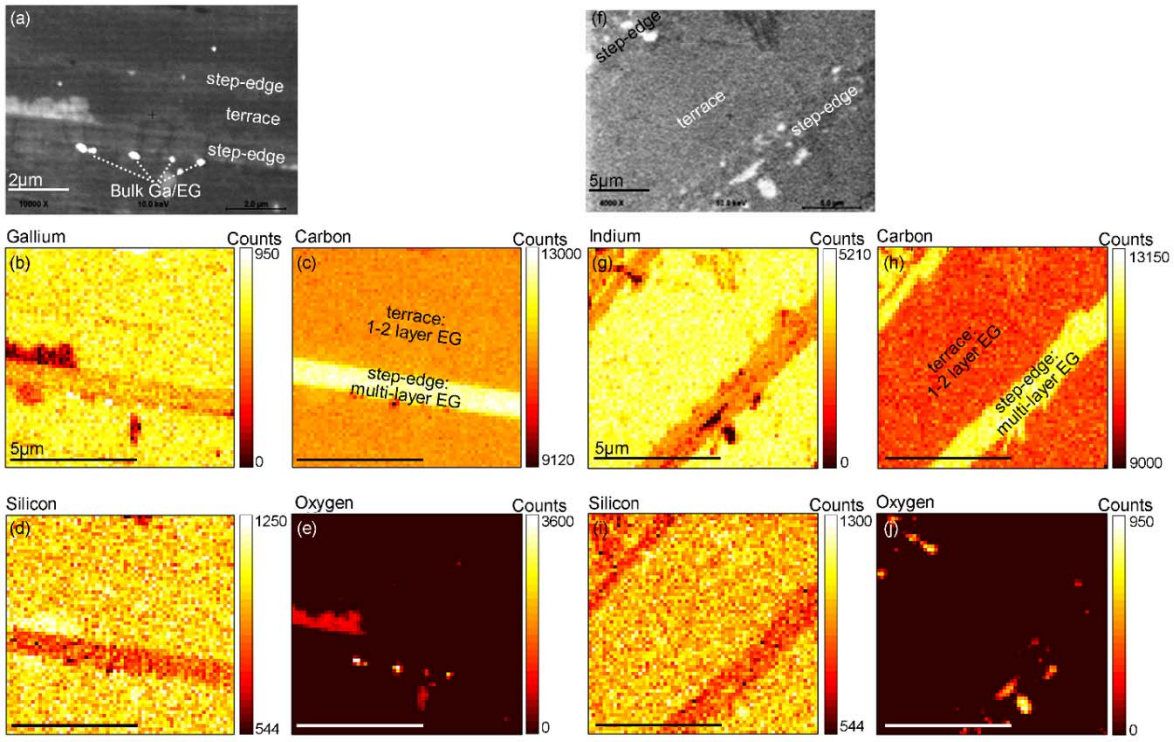

Figure S3: Auger electron spectroscopy maps of EG/Ga/SiC and EG/In/SiC samples and corresponding scanning electron microscope images. Ga, In, C, Si, and O are shown in the AES maps, which display terrace and step-edge regions for both samples. Step-edges show stronger relative C signal, which could indicate greater numbers of EG layers that attenuate the signal of the underlying Si and metal layers. Small, O-rich regions are observed near step edges, where some metallic islands have nucleated on top of the EG layers.

nucleated on top of EG layers near step edges. The oxygen-rich, circular features shown in S3(e) correspond to metal-rich regions shown in S3(b). However, some oxygen-rich regions correspond to areas with decreased metal signal regions (S3(e) vs. (b), S3(j) vs. (g)). These regions could contain a silicon oxide and/or fewer EG layers, allowing for local oxygen penetration. The chemistry of these regions is still under investigation.

Raman Spectroscopy

Figure S4 displays Raman maps for three different monolayer EG/Ga samples including partially Ga-intercalated samples prepared using as-grown EG (small-step SiC) and fully Ga-intercalated samples prepared using plasma-treated EG (and both small and large step SiC). For all EG types, the G:2D ratio is the starkest means for identifying Ga-intercalated regions due to the G peak enhancement, which corresponds with optical contrast observed in S4(a). Intercalated regions also display increased area under the curve (i.e. full-width-half-maximum) for both G and 2D peaks compared to as-grown EG due to the conversion of buffer layer to an additional layer of EG via intercalation. Regardless of initial step-morphology, plasma-treatment of the EG layers prior to intercalation results in an EG/Ga film with a uniform G:2D ratio across the mapped area (Figure S4(b, f)), indicative of uniform Ga intercalation. These results are consistent with Auger mapping and other characterization.

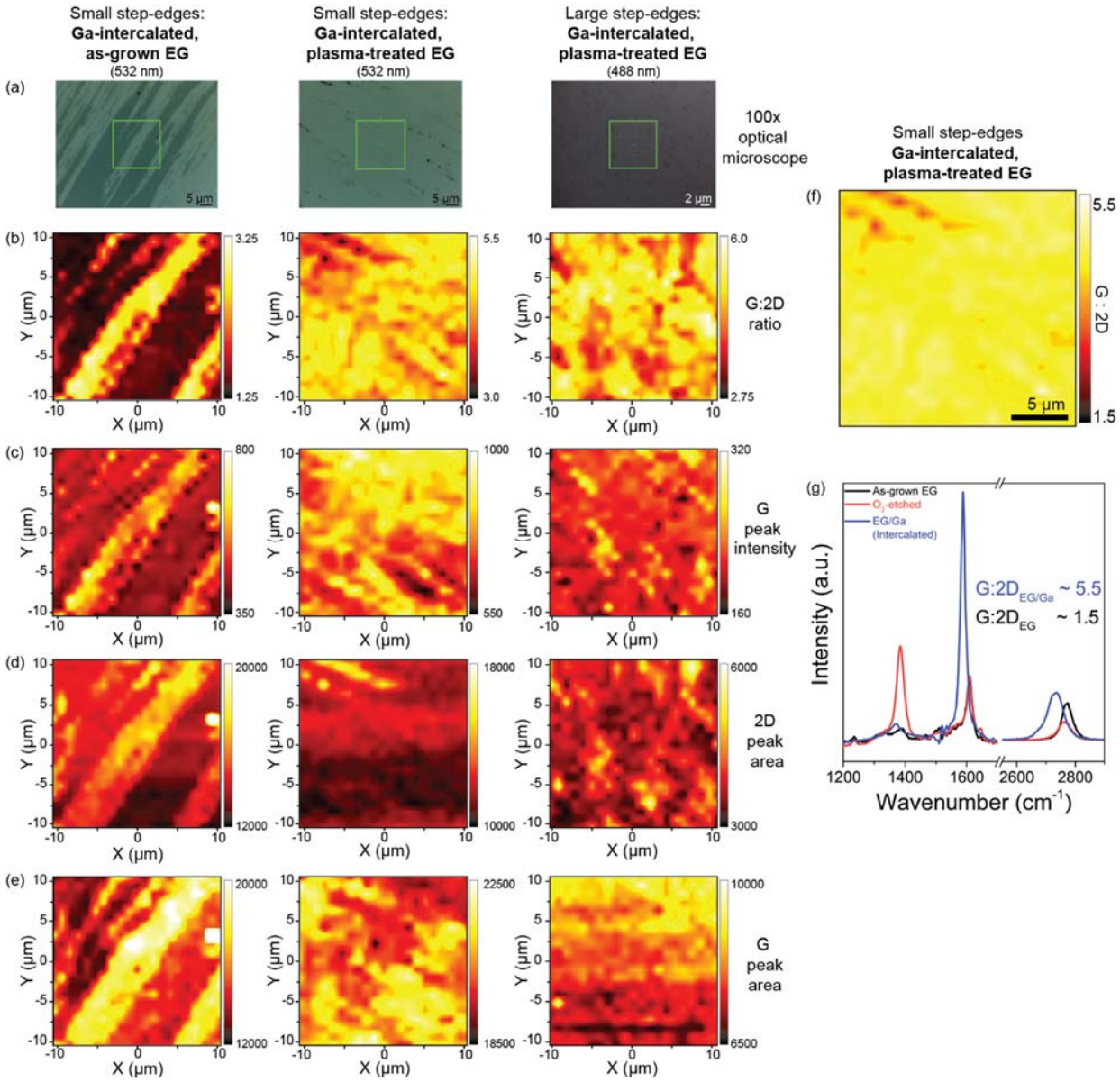

Figure S4: Raman mapping of EG/Ga samples. (a) Optical microscope images of three intercalated monolayer EG/Ga films synthesized from different EG/SiC types including as-grown EG (small step morphology), plasma-treated EG (small step morphology), and plasma-treated EG (large step morphology). The green box in the center of the OM images indicates where the following 20×20 μm Raman maps (1 μm step size) were collected: (b) G:2D peak intensity ratio, (c) G peak intensity, (d) 2D peak area-under-the-curve, and (e) G peak area-under-the-curve maps. (f) G:2D map of plasma-treated EG (small-step sample) with color scale re-normalized from 1.5 to 5.5, which effectively brackets the G:2D range from pre and post intercalation. All maps in (b-e) are automatically normalized individually in the Horiba Labspec software based on their individual intensity count histograms. Their respective scale bars and intensities are shown. (g) Representative Raman spectral evolution from as-grown EG to plasma-treated EG to intercalated EG, showing the relative change in peak line-shapes, positions, and intensities. The Raman data from (g) are taken from a large-step EG/SiC sample. 532 nm laser (~12 mW) was used for the first two columns of maps in (a-e) (small-step EG/SiC), while 488 nm (~5 mW) was used for the third column of maps in (a-e) (large-step EG/SiC).

Modeling of Graphene Defects and Ga Bonding

Following experimental validation of basic defect chemistry, the binding energies of Ga atoms to graphene defect sites were examined. Ga atoms were supported on optimized graphene sheets with bare and O– and OH– passivated defects, separately. This resulted in twenty models that were allowed further structural relaxation. Figure S5(a-v) illustrates the optimized structures. The adsorption energy, E_{ads}, of a Ga atom was computed based on Eq. 4 where E_{Gr+Ga} is the total energy of the graphene with a Ga atom adsorbed. E_{Gr} and E_{Ga} are the energies of the graphene sheet and an isolated Ga atom in a vacuum, respectively.

$$E_{ads} = E_{Ga+Gr} - (E_{Gr} + E_{Ga}) \quad (4)$$

As depicted in Figure S5(w, y), the adsorption of a Ga atom on a graphene sheet is an exothermic process. The existence of the bare defect enhances the binding strength of Ga atom to the graphene layer as a consequence of the increase in the number of the under-coordinated edge-carbon atoms surrounding the defects (Figure S5(a-d, j-m, w)). These results reveal that the bare defect can strongly bias trapping Ga atoms in graphene by forming a covalent bond with the Ga atom with large binding energy (7.38 eV). However, this, in turn, may cause an inability to release the Ga atoms from these defects since breaking the C–Ga bond would require a high dissociation energy. On the other hand, passivating the dangling bonds around the edge of the bare defects with O or OH groups significantly weakens the binding strength of Ga to graphene. O–passivated defects still show higher Ga binding energies than that of pristine graphene (>1.75 eV) as illustrated in Figure S5. This indicates that defects still serve as binding sites for Ga atoms and may also allow de-trapping of Ga atoms from the graphene sheet with relatively low dissociation energies. The behavior of Ga binding to passivated, defective graphene also shows a discrepancy in terms of the O–induced bond and vacancy type: the odd-numbered vacancy defects (Figure S5(n-r)) bind Ga more strongly than the even-numbered ones (Figure S5(e-i)) owing to the existence of out-of-plane C=O double bonds which act as trapping centers for the Ga atom (Figure S5(w-II, y-I)). Contrary to the carbonyl (C=O) bond formation, the ether (C–O–C) groups (where carbon atoms exhibit an sp^2 hybridized form) are capable of contributing to the stabilization of the even-numbered defects by the pair-wise removal of the unsaturated bonds (Figure S5(e-i, w-II). There is also an evident trend between the vacancy size and the binding strength of the Ga atom. As depicted in Figure S5(w-II), octa- and hepta-vacancy defects have highest binding energies of 2.08 and 3.36 eV, respectively, among the even- and odd-numbered vacancy types, indicating that the vacancy size plays a crucial role in tuning the defect/metal interaction, and can enable control over Ga intercalation. When the edge atoms in question are saturated with OH– groups in the odd-numbered defects (Figure S5(s-v)), the C–O–H bond formation dramatically alters the binding strength of Ga atom, and can result in lower binding energy even than that of the pristine graphene (<1.75 eV). As depicted in Figure S5(t, u) and Figure S5(y-II), tri and penta-vacancy defects saturated with OH– groups only weakly attract the Ga metal atoms, with the energies of 1.41 eV and 1.35 eV, respectively. This specifies that the defects saturated with OH– are unable to draw Ga atoms to the surface and may cause a clustering between the Ga metals. Such a weak interaction between graphene and metal atoms may have a detrimental effect on Ga intercalation. Note that mono and hepta-vacancies in Figure S5(s,v) have higher binding energies than pristine graphene since in these cases the Ga atom interacts with O atoms instead of the H atom.

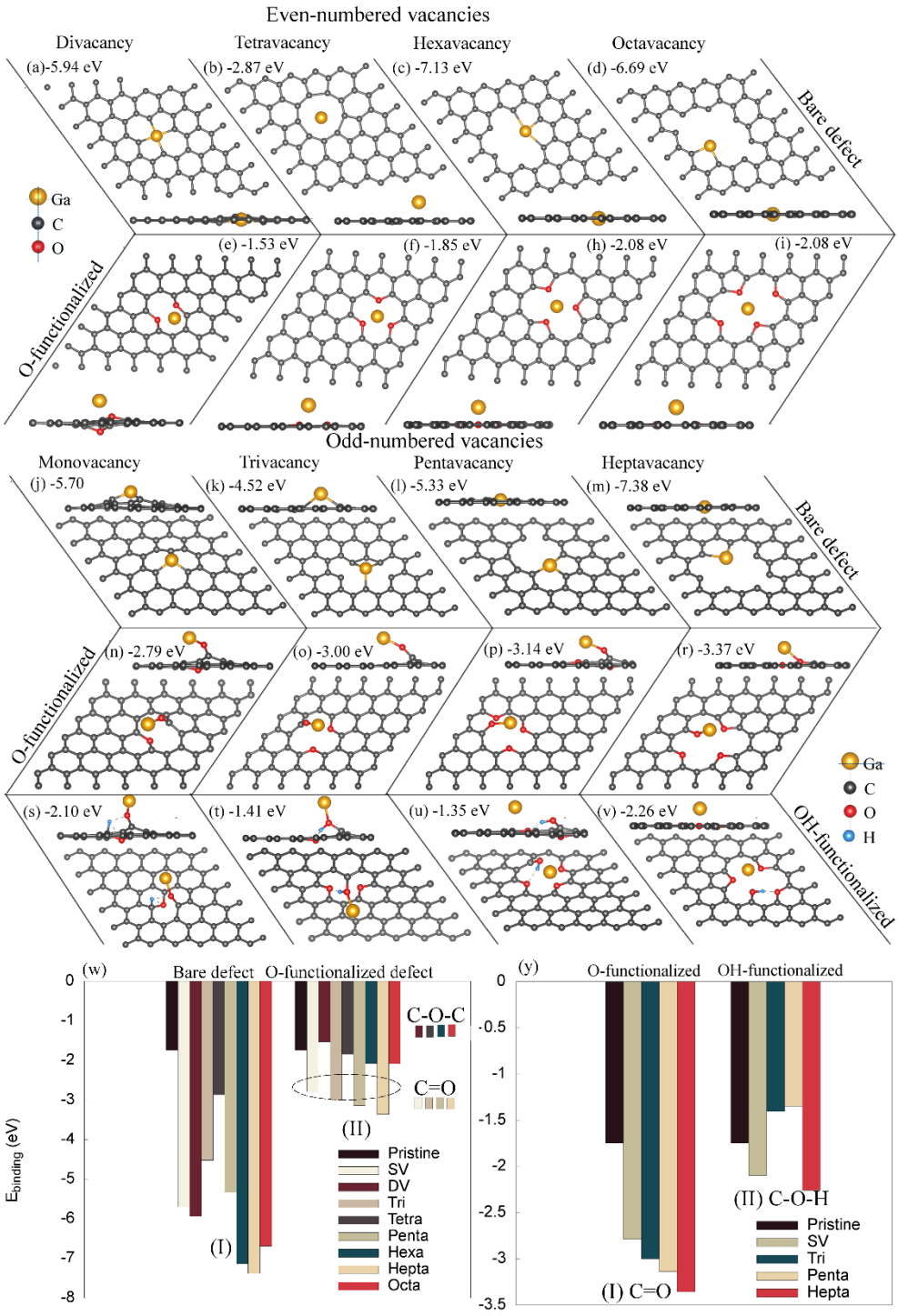

Figure S5: Ball-and-stick representation of Ga adsorbed onto graphene with (a-d, j-m) bare defects, (e-i, n-r) O– and (s-v) OH–passivated defects where their individual binding energies are presented. (e-i) correspond to C=O passivation and (n-r) correspond to C–O–C passivation. (w, y) Binding energies of Ga to defective graphene with/without the functional groups where (w-I) corresponds to bare defects, (w-II) bars with light and dark colors correspond to C=O and C–O–C, respectively, (y-I) corresponds to C=O, and (y-II) corresponds to C–O–H. Defect types are monovacancy (SV), divacancy (DV), trivacancy (Tri), tetravacancy (Tetra), pentavacancy (Penta), hexavacancy (Hexa), heptavacancy (Hepta) and octavacancy (Octa).

2D Metal Phase Stability

The phase stabilities of 1 layer, 2 layer, and 3 layer metals (in red, green, and blue lines) discussed in the main text and in Figure 2 do not include a bilayer graphene cap. The cases when bilayer graphene is included are shown in Figure S6. For Ga and In the results are qualitatively unchanged: the allowed range of metal chemical potentials would yield 1, 2, or 3 layers of Ga and 1 or 2 layers of In. For Sn, although the trilayer stabilizes itself against the monolayer structure near the bulk Sn chemical potential by relaxing into a simple-hexagonal $Sn_{Si}Sn_{Si}Sn_{Si}$ stacking, the higher-energy bilayer structure within the same chemical potential range (relaxed into a distorted structure where Sn atoms in the second Sn layer are no longer coplanar) may kinetically prevent the system from accessing the trilayer structure. This is consistent with the blurred STEM images of the second Sn layer discussed in the main text.

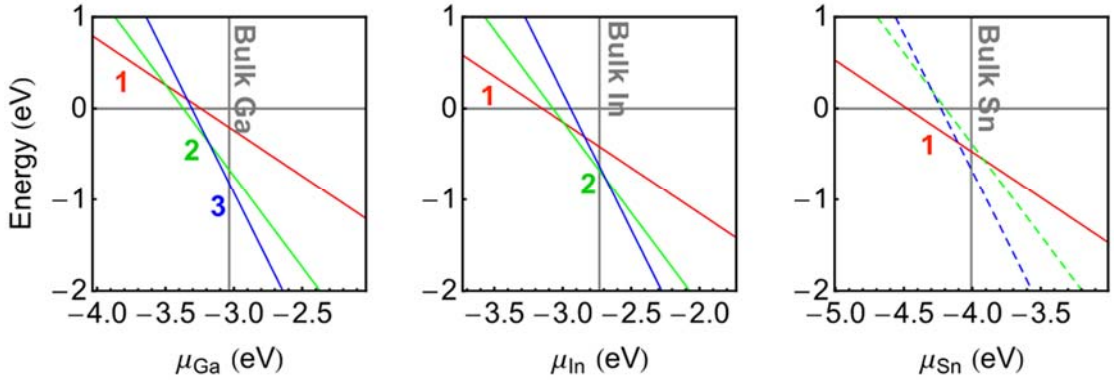

Figure S6: Phase stability of 1 layer, 2 layer, and 3 layer metals as functions of metal chemical potentials, with a bilayer graphene cap included

Energy-dispersive x-ray spectroscopy

Energy-dispersive x-ray spectroscopy maps show the distribution of metal, Si, C, and O within cross-sectional samples. C signal is observed from SiC and epitaxial graphene layers. Oxygen signal is observed from the top-most, protective silicon dioxide coating. Si is observed from SiC and the silicon dioxide. Metal signal (Ga, In, Sn) signal is observed between C/Si signal in SiC and C signal in epitaxial graphene.

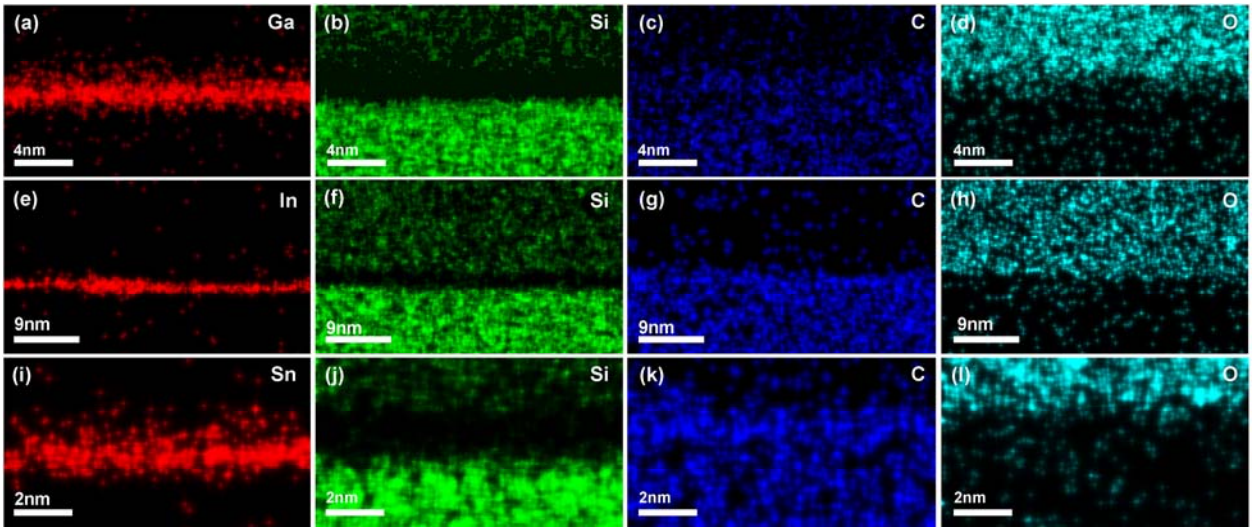

Figure S7: Energy dispersive x-ray spectroscopy maps collected for Ga, In, and Sn intercalated EG samples. Oxygen signal is located above intercalant layers, indicating the metal films are not oxidized.

Low-energy electron diffraction

Low-energy electron diffraction of EG/SiC shows diffraction spots corresponding to SiC, graphene, and the $6\sqrt{3}\times6\sqrt{3}$ R30° reconstruction layer present in EG grown on SiC. Upon intercalation, the reconstructed layer is lifted, and the EG/SiC is converted to quasi-freestanding EG. The intercalated systems exhibit diffraction spots for EG and SiC only.

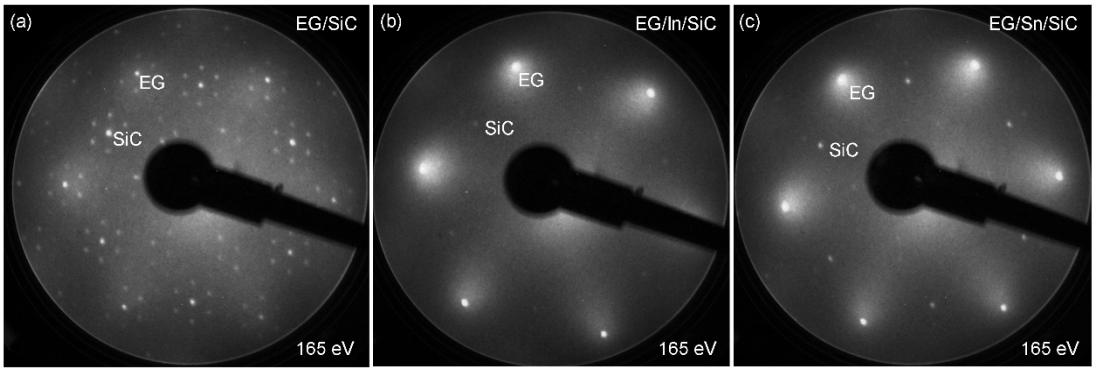

Figure S8: Low energy electron diffraction patterns for EG/SiC, EG/In/SiC, and EG/Sn/SiC acquired at 165eV. Additional spots in EG/SiC pattern correspond to buffer layer reconstruction.

2D Ga spacing

Imagej analysis of a cross-sectional scanning transmission electron microscope image of intercalated Ga on SiC shows the spacing of Si atoms in SiC (d ~ 2.70Å) is close to that of Ga atoms (d ~ 2.72Å)

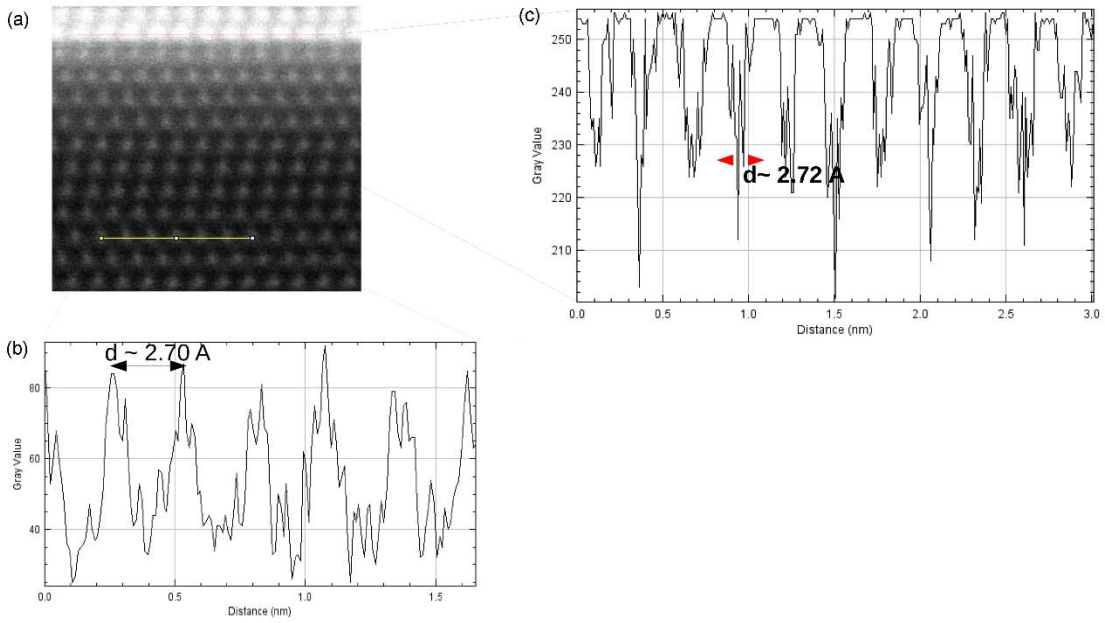

Figure S9: Cross-sectional STEM image of Ga/SiC, where SiC atoms across the yellow line show a spacing of 2.70Å, and the Ga atoms across the red line show a spacing of 2.72Å

Ga stacking order at the bilayer graphene/SiC interface

The thermodynamic ground states for bilayer and trilayer Ga are discussed in the main text without including a capping bilayer graphene. The relative energies of all possible bilayer structures are listed in Table S1 under "w/o graphene cap", where Site 2 lies further away from the SiC surface than Site 1. By including a bilayer graphene cap (necessitating a larger 2×2 bilayer graphene + √3×√3 R30º Ga/SiC supercell), the order of the relative energies is not altered, as shown under "with graphene cap". The same applies for the trilayer case, with the following exception. The $Ga_CGa_{hollow}Ga_{hollow}$ and $Ga_{hollow}Ga_{Si}Ga_{Si}$ structures become unstable when the capping bilayer graphene is added and transform to $Ga_{Si}Ga_{hollow}Ga_C$ and $Ga_{Si}Ga_CGa_{Si}$ respectively. The energies of the original unstable structures (marked by asterisks) are estimated using a force convergence threshold (0.05 eV/Å) larger than that enforced for every other case (0.01 eV/Å). Even with these exceptions the ground state is still $Ga_{Si}Ga_CGa_{hollow}$.

Table S1: Relative stability per unit cell (i.e. per 8.30 $Å^2$) of possible stacking orders of bilayer and trilayer Ga, following the notation of $Ga_{site1}Ga_{site2}Ga_{site3}$… with site indices increasing further away from the Si/Ga interface. See text for the discussion on locally unstable structures with energies marked by asterisks.

Site 1	**Site 2**	**w/o graphene cap**	**with graphene cap**
C	Si	0.56	0.54
C	C	0.51	0.49
C	Hollow	0.47	0.45
Hollow	Si	0.45	0.43
Hollow	Hollow	0.42	0.42
Hollow	C	0.3	0.30
Si	Si	0.22	0.23
Si	Hollow	0.05	0.05
Si	C	0	0

Site 1	**Site 2**	**Site 3**	**w/o graphene cap**	**with graphene cap**	**local instability**
C	Hollow	Hollow	0.58	0.58*	0.02 (→Si hollow C)
Hollow	Si	Si	0.49	0.50*	0.04 (→Si C Si)
C	Hollow	Si	0.46	0.45	
Hollow	Si	C	0.35	0.36	
Si	C	C	0.04	0.04	
Si	C	Si	0.03	0.02	
Si	C	Hollow	0	0	

Band structures at the PBE level and hybrid functional level

Figures S10-11 show calculated band structures for bilayer and trilayer Ga on SiC. These calculations are compared with experimental ARPES measurements (main text Figure 3) to find the most favorable 2D-Ga structures. Among the bilayer band structures, the $Ga_{Si}Ga_{C}$ case achieve the best agreement in terms of relative band positions, with the only exception that the Fermi energy appears to be off by 0.6 eV. For trilayers, the $Ga_{Si}Ga_{C}Ga_{C}$ and $Ga_{Si}Ga_{C}Ga_{hollow}$ band structures both show some deviations near K but match with additional bands with weak intensities in ARPES and have Fermi level in alignment with the ARPES measured one. Two other geometries with extra carbon atoms near the Ga/SiC interface were also considered but gave drastically different band structures.

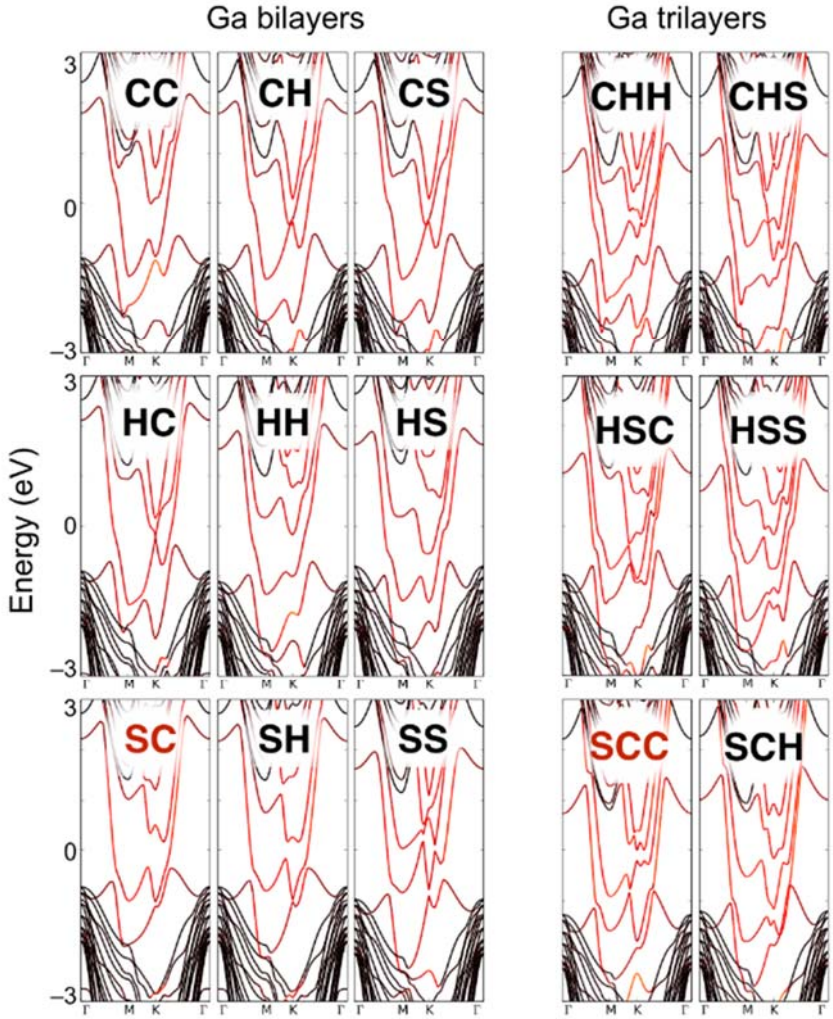

Figure S10: Projected band structures for all possible bilayer Ga geometries and for selected trilayer Ga geometries calculated at the DFT level, where Ga orbital characters are indicated in red. The best matching case for bilayer and trilayer are $Ga_{Si}Ga_{C}$ and $Ga_{Si}Ga_{C}Ga_{C}$ (highlighted in red). This is consistent with $Ga_{Si}Ga_{C}$ being thermodynamic ground state for the bilayer case and $Ga_{Si}Ga_{C}Ga_{C}$ being the nearly-degenerate next-lowest-energy structure for the trilayer case. "S", "C", and "H" in S10 refer to the silicon, carbon, and hollow sites of SiC (trilayer Ga $Ga_{Si}Ga_{C}Ga_{C}$ corresponds to the band structure labeled SCC).

For the best matching cases, bilayer $Ga_{Si}Ga_{C}$ and trilayer $Ga_{Si}Ga_{C}Ga_{C}$, we performed additional band structure calculations at the hybrid functional level (HSE06, see Methods) to rule out the possibility that the above band structure deviations could be due to the intrinsic delocalization error of approximate functionals at the DFT level. As shown in Figure S11, we observe an overall energy rescaling that increases the bandwidth of the metal by expanding states away from the Fermi level. For the case of bilayer Ga, the leftmost band crossing point along Γ–M lowers away from the Fermi level, from –0.6 eV in the DFT (PBE functional) case to –1.1 eV in the hybrid functional case. The latter energy separation matches with the ARPES measured one (–1.2 eV) better, thus removing the need to impose an artificial Fermi level shift as discussed in the main text. Thus we conclude that the dominant surface phase is bilayer $Ga_{Si}Ga_{C}$ geometry, consistent with it being the ground state of bilayer Ga, likely with co-existing $Ga_{Si}Ga_{C}Ga_{C}$ structures.

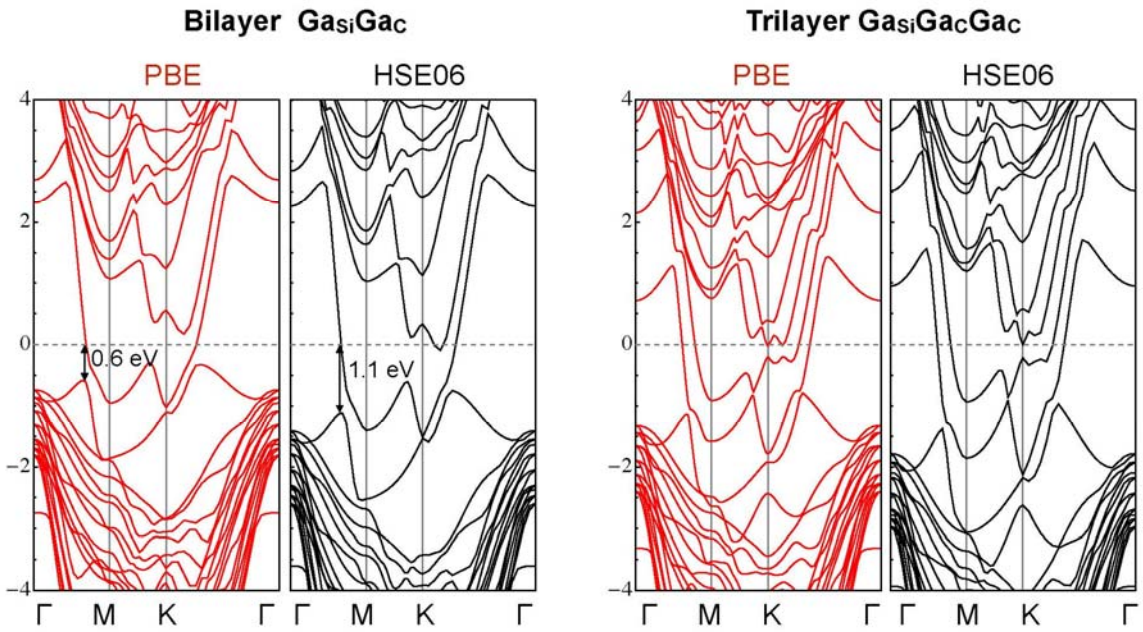

Figure S11: Band structure for the (left) $Ga_{Si}Ga_{C}$ bilayer and the (right) $Ga_{Si}Ga_{C}Ga_{C}$ case calculated at DFT and hybrid functional (HSE06) levels.

Angle-resolved photoemission spectroscopy of 2D In

ARPES measurements of In-intercalated, plasma-treated EG. The measurements resemble those of Ga/SiC in main text Figure 3, where the sample exhibits graphene bands near K_g, in addition to avoided band crossing points of In along Γ–M_{Ga} and Γ–K_{Ga}. Additionally, the graphene BZ zone is 30° rotated from that of the In/SiC BZ.

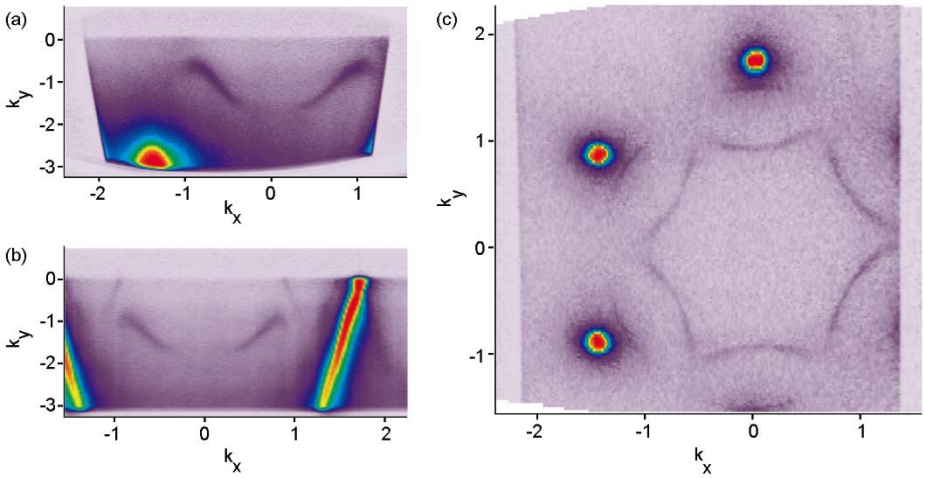

Figure S12: ARPES measurements of EG/In/SiC, showing similarities to EG/Ga/SiC measurements in the form of EG bands, avoided crossing points, and an In/SiC BZ rotated 30° from EG.

Calculated band structure of bilayer Ga

The approach used for ARPES discussion accompanying Figure 3 in the main text is as follows: we construct a 2×2 graphene + √3×√3 R30º Ga/SiC supercell; its deviation from the ideal 13×13 graphene + 6√3×6√3 R30º Ga/SiC supercell induces an 8% artificial strain to the graphene lattice and a consequential ~0.5 eV increase in its work function.[6] Thus, we only compare selected band features with ARPES in the first approach, whereas band alignment between Ga and graphene could be off by 0.5 eV. For the second approach, we construct a 5×5 graphene + 4×4 R0º Ga/SiC supercell. Although the relative interfacial orientation is incorrect, this supercell avoids the creation of the artificial interfacial strain and should yield more accurate charge transfer and band alignments. The resulting doping level of graphene for bilayer and trilayer Ga are 0.15 and 0.42 eV, consistent with the work function variation between the two: 4.61 and 4.06 eV for bilayer and trilayer Ga. Thus it appears that whereas band features more closely resemble the calculated bands for bilayer Ga, the band alignment and filling suggests the presence of trilayer Ga.

To reveal the orbital origin of the band crossing along Γ–M_{Ga} in Figure 3a,b, we compare the projected band structure of bilayer Ga/SiC (without graphene) to a hypothetical freestanding bilayer Ga where Ga atoms are frozen at their positions in the hybrid system, as shown in Figure S13. The latter clearly shows three nearly-free-electron-like bands of *s*-bonding (green), *s*-antibonding (blue), and *p* (red) orbital character. The band crossing is thus hybridization between a parabolic *s* orbital originating from ~9 eV below the Fermi level and the *p* orbital near the Fermi level. Similarly, the band crossings along Γ–K_{Ga} are also between *s* and *p*.

To verify whether the 2D Ga is under in-plane epitaxial strain, we calculated the Ga contribution to the total strain energy of the hybrid system by subtracting the contribution of the bare SiC substrate from the total. The minimum strain energy occurs at 95% and 96% of the in-plane lattice constant of SiC (0001) for bilayer and trilayer Ga. Thus, the Ga region is under moderate tensile strain.

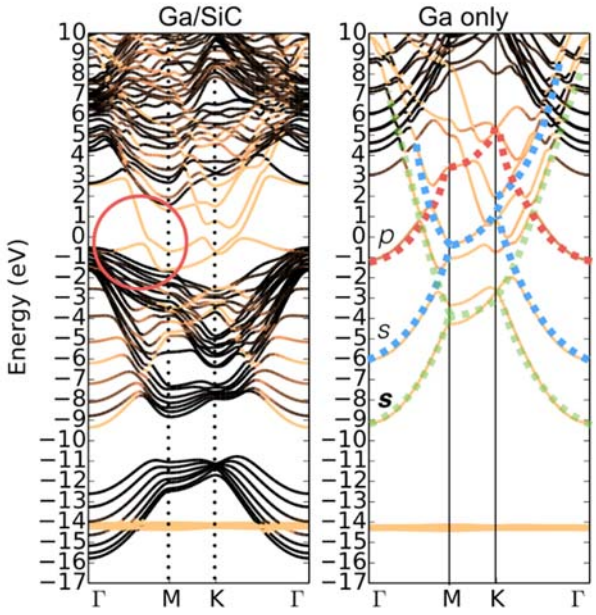

Figure S13: DFT band structure of bilayer Ga/SiC without graphene. Comparing with the bands of hypothetical freestanding bilayer Ga (right panel), the origin of the bands with Ga orbital characters colored in orange can be assigned *s* bonding (green), *s* antibonding (blue), and *p* (red) characters. The *s* band with the deepest level origin contributes most to the Fermi surface.

Angle-resolved photoemission spectroscopy of epitaxial graphene in EG/Ga/SiC

ARPES measurements of the EG K-point for EG/Ga/SiC show the E_F–E_D = ~ 0.2–0.3 eV. For reference, as-grown EG/SiC E_F–E_D = ~ 0.42 eV[7]. Hydrogen-intercalated EG E_F–E_D = ~ –0.1 eV[7].

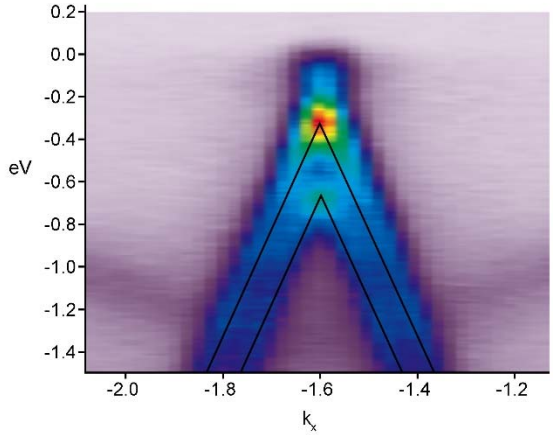

Figure S14: Acquired ARPES data showing the EG K-point for an EG/Ga/SiC sample, with E_F – E_D = ~0.2–0.3eV, indicating that the EG is n-doped by approximately 8–10×10^{12} cm^{-2}.

Estimating upper critical fields

Figure S15 shows B_{c2} vs. temperature data extracted from the data shown in main text Figure 4c. B_{c2} is defined as the critical field at 90% of the normal resistance. The data is fitted to the phenomenological 2D and 3D Ginzburg–Landau (GL)[8] models to extract an approximate B_{c0}.

The phenomenological 2D Ginzburg–Landau (GL) model is given by:

$$B_{c2}(T) = B_{c0}\left(1 - \frac{T}{T_c}\right)$$

The 3D-GL parabolic relationship is given by:

$$B_{c2}(T) = B_{c0}\left(1 - \left(\frac{T}{T_c}\right)^2\right)$$

The variation between these models can be considered to reflect an uncertainty in the precision of the extrapolation.

Transport in small-step 2D Ga samples

R(T) and R(B) data is shown in S15(b, c) for small step, Ga-intercalated plasma-treated EG samples. After initial measurements, samples are removed from the physical property measurement system (PPMS) system. This may lead to oxidation of scratched regions where In dots contact exposed 2D Ga layers, and could be the cause of increased resistance observed for subsequent measurements (dotted lines in S15(b, c)). Additionally, two superconducting phases likely exist in the samples. This could be due to interactions between step-edges, variation in Ga layer number, or distinct superconducting transitions within a single 3 layer region.

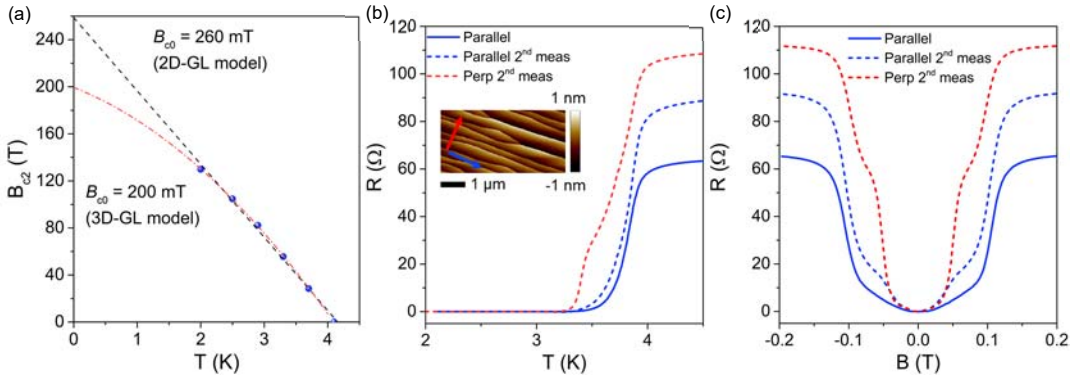

Figure S15: Transport in small-step EG/Ga samples. (a) Plot of critical field (B_{c2}) vs. temperature, extracted from R(B) data in Figure 4c. Here, B_{c2} is defined as the critical field at 90% of the normal resistance. The data is fitted to the phenomenological 2D and 3D Ginzburg–Landau (GL) models to extract an approximate B_{c0}. (b, c) Subsequent R(T) and R(B) curves in small-step EG sample, displaying increased resistance for the second measurement (dashed blue line). In the case of these measurements, samples are completely removed from the PPMS system between measurements. The increase in resistance may be due to oxidation at the scratched edge regions where In dots are contacting exposed Ga. There likely exists two distinct superconducting phases in these samples, possibly due to step-edge interactions, thickness differences (2 vs 3 layer Ga), or to two distinct superconducting transitions within a 3 layer Ga region. Both 2 and 3 layers of Ga have been observed across individual SiC terraces.

Scanning tunneling microscopy and spectroscopy (STM & STS)

A variety of EG/Ga surface topographies are shown via scanning tunneling microscopy. S15(a) shows a superconducting terrace region containing island-like defects. Carbon vacancies such as the one in S15(d) are also observed. S15(e) shows a partially intercalated region, where the red dot corresponds to a region containing Ga. These regions do not show a superconducting energy gap from STS.

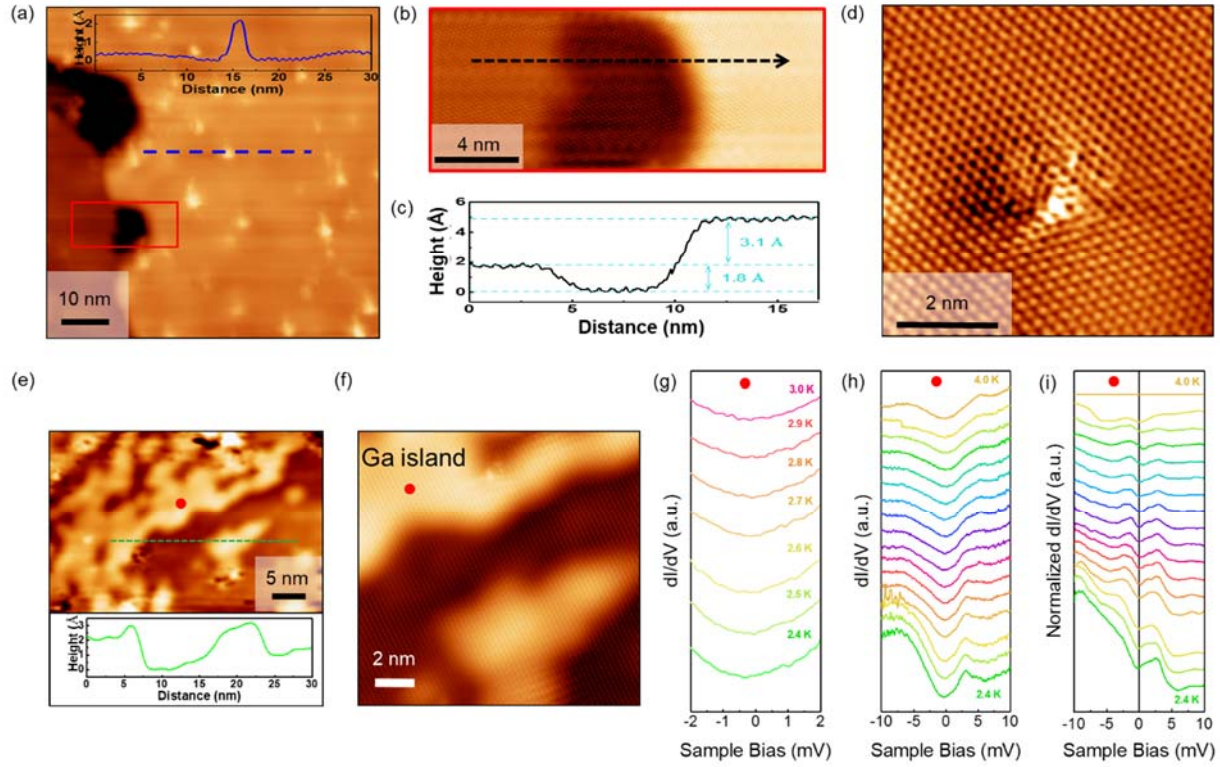

Figure S16: STM/STS of fully and partially intercalated EG/Ga films. (a) STM image of a superconducting EG/Ga heterostructure film (V_b = 10 mV and I_t = 400 pA). Inset at the top of (a) is a height profile of the dashed blue line intersecting a 2 Å tall defect observed in superconducting terrace regions. The origin of these "island" defects is unknown. (b) A zoomed-in STM image of a step-edge region (V_b = -200 mV, I_t = 200 pA) where STS spectra and superconducting energy gaps were measured. (c) A height profile of the dashed black line in (b), showing relatively small step-height of several angstroms. (d) High-magnification STM image of the EG surface with a carbon vacancy in the center, as evidenced by the triangular distortions around the center (V_b = -100 mV, I_t = 100 pA). (e) STM image of a partially intercalated EG/Ga film (V_b = 1.0 V, I_t = 400 pA). Inset: height profile corresponding to the dashed green line in (e). (f) Zoomed-in STM image of the area shown in (e) (V_b = 1.0 V, I_t = 100 pA). The EG lattice is observed across the image, indicating the topography is due to partial Ga intercalation (possibly 1 Ga atom). (g-i) Temperature dependent dI/dV spectra at the red mark in (e-f) (V_b = 10 mV, I_t = 400 pA, and ΔV = 0.1 mV) for different energy ranges. Note that the spectra in (h) are the same as in (g) but over a wider bias range and curves from 3 – 4 K are also displayed for thoroughness. No clear superconducting energy gap with coherence peaks is observed for partially intercalated Ga islands. (i) dI/dV spectra in (h) normalized by 4.0 K curve.

Extraction of transition temperatures

The Berezinskii–Kosterlitz–Thouless (BKT) transition temperature is extracted for both parallel and perpendicular current directions (Figure S17(a,b), where 2D superconductivity is characterized by a transition from $V \propto I$ in the normal state to $V \propto I^{\alpha}$ in the superconducting state, and the temperature at which $\alpha=3$ is defined as T_{BKT}[9] (Figure S17(c)). Here, $T_{BKT} = 3.1$ K (2.9 K) for the parallel (perpendicular) configuration in small-step 2D-Ga. Although the actual T_{BKT} is likely higher if the power law exponents are curve-fitted closer to the critical current I_c[9,10], the similar T_{BKT} observed for both current directions indicates nearly isotropic transport in 2D-Ga/SiC. A plot of $d\ln(R)/dT)^{-2/3}$ vs T indicates a $T_{BKT} = 3.88$ K (Figure S17(d)), which reinforces the observation that the T_{BKT} values extracted from the I-V curves in Figures S17(a,b) represent lower-bound estimates and are limited by the measurement setup. The power-law fitting for the T_{BKT} extraction was done in the lower current and voltage regime (near the bottom of each curve) as we were not able to measure the full I-V curves up to the critical current I_c and into the normal state (following $V \propto I$) due to PPMS current/voltage limitations. Because of this, T_{BKT} is likely higher than 3.14 K if the power-law exponent curve fitting is done closer to I_c where the slope is usually steepest, as is reported in other works.

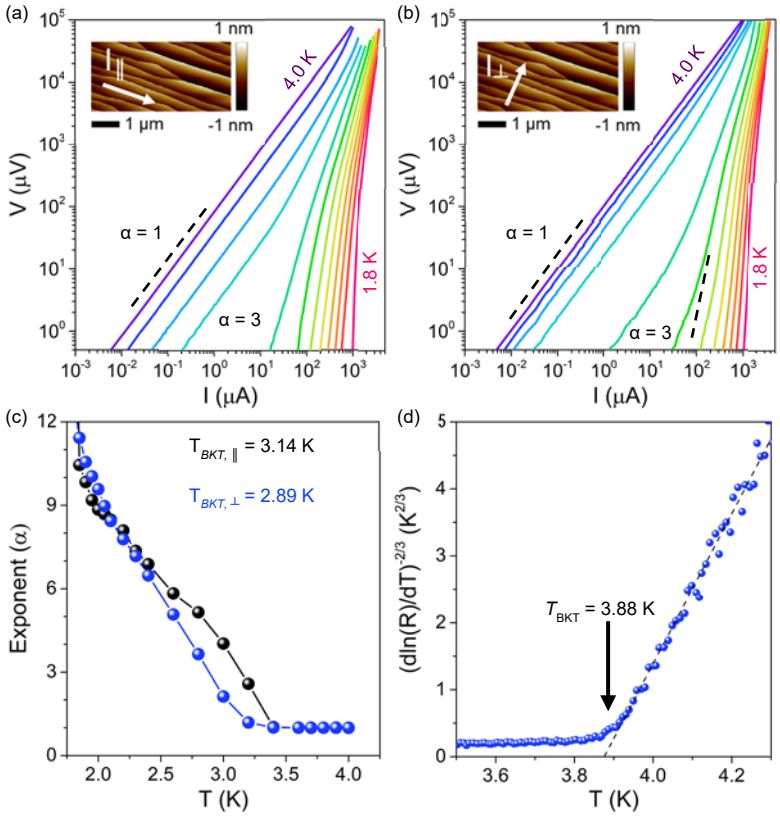

Figure S17: BKT transition in small-step EG/Ga. (a, b) Current-voltage (I-V) curves measured in parallel and perpendicular current directions, respectively, on the same small-step EG/Ga sample. (c) Exponent (α) vs temperature plots for both measurement directions displaying the lower-end estimates of the BKT transition temperatures. (d) Plot of $[d(\ln R)/dT]^{-2/3}$ vs. T, showing the extrapolated BKT transition (T_{BKT}) temperature from R(T) measurements, specifically the zero-field curve for small-step EG/Ga.

Transport in large-step 2D Ga

Transport data for large-step 2D Ga samples is shown in S18. S18(c) shows a comparison of R-T data for Ga-intercalated as grown and plasma-treated EG samples with large steps. Large-step Ga-intercalated, as-grown EG samples do not exhibit a superconducting transition. R-T measurements taken perpendicular to the step-edge direction show a broader transition than those taken parallel to the step-edge direction (S18(f)). When measuring a second time in the perpendicular direction, large-step samples do not reach zero resistance. This is believed to be due to oxidation at scratched edges, as discussed in Figure S15.

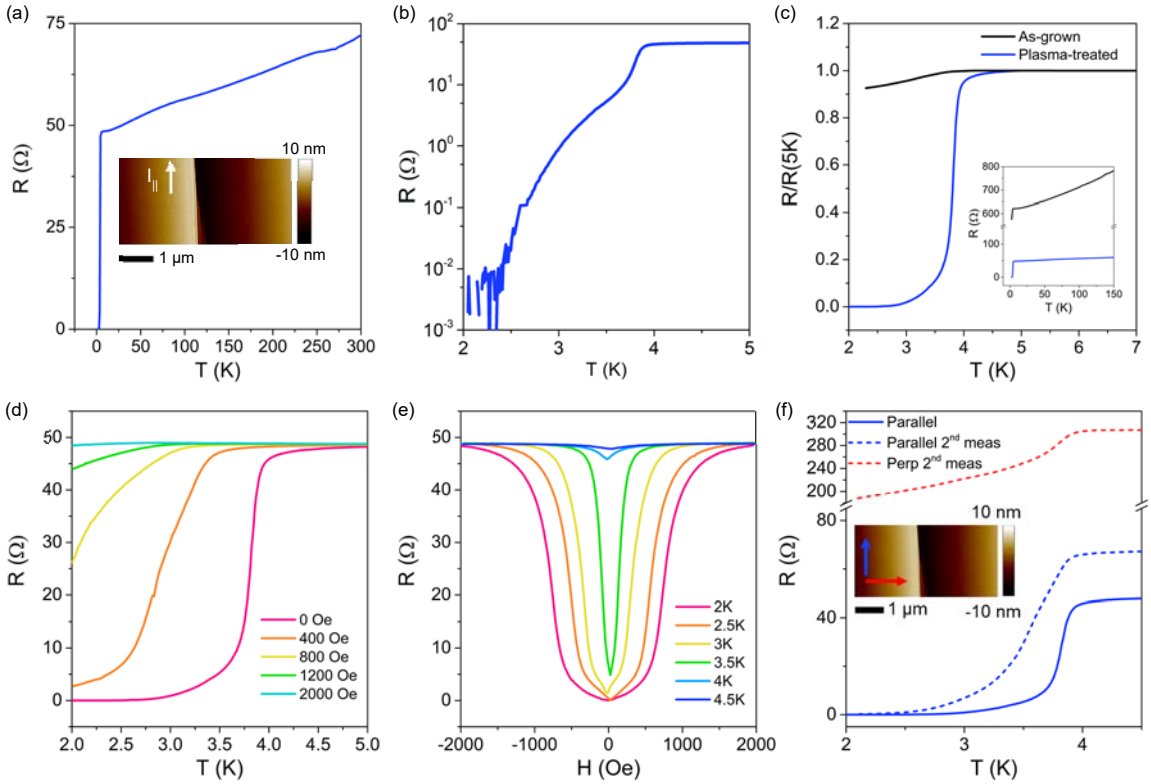

Figure S18: Transport in large-step EG/Ga samples. (a) Zero-field R(T) curve from 2 K – 300 K, displaying metallic behavior and a full superconducting (SC) transition at low T. Inset: AFM image of large-step EG/SiC morphology. (b) Log-scale R(T) from 2 K-5 K replotted from (a). (c) R(T) curves (normalized to R(5 K)) for large-step EG/Ga synthesized from as-grown EG (non-plasma-treated) and plasma-treated EG, showing the importance of plasma-treating EG layers (prior to intercalation) in achieving macroscopically coherent superconductivity. (d, e) Typical R(T) and R(B) curves showing a breakdown in the superconducting phase with increasing perpendicular magnetic field and temperature. (f) Zero-field R-T measurements for a large-step 2D Ga sample, showing differences between initial and subsequent measurements. In the case of these measurements, samples are completely removed from the PPMS system between measurements. Increased resistance may be due to oxidation at the scratched edge regions where In dots are contacting exposed Ga.

Details on electron-phonon coupling computations

To estimate T_c of 2D-Ga from first-principles, we calculate electron-phonon (el-ph) coupling strength λ derived from the Eliashberg spectral function $\alpha^2F(\omega)$ for a 3 layer-Ga/SiC system without the graphene cap. Achieving a converged Eliashberg spectral function relies on a dense k-point sampling of el-ph matrix elements, as realized using Wannier-Fourier interpolation[11] (Figure S19(b)). The Eliashberg spectral function, in the isotropic formalism, is given by $\alpha^2F(\omega) = (1/2N_F) \Sigma_{\boldsymbol{kq}\nu} |g_{mn}{}^{\nu}(\boldsymbol{k},\boldsymbol{k}+\boldsymbol{q})|^2 \delta(\varepsilon_{n,\boldsymbol{k}}) \delta(\varepsilon_{m,\boldsymbol{k}+\boldsymbol{q}}) \delta(\omega-\omega_{\boldsymbol{q}\nu})$, where N_F is the density of states at the Fermi level, $g_{mn}{}^{\nu}(\boldsymbol{k},\boldsymbol{k}+\boldsymbol{q})$ is the el-ph matrix elements characterizing electrons scattering from state $(n,\boldsymbol{k})$ to state $(m,\boldsymbol{k}+\mathbf{q})$ by a phonon of mode ν, with their respective energies given by $\varepsilon_{n,\boldsymbol{k}}$, $\varepsilon_{m,\boldsymbol{k}+\boldsymbol{q}}$ (measured from the Fermi level) and $\omega_{\boldsymbol{q}\nu}$. The cumulative el-ph coupling strength is given by $\lambda(\omega) = 2\int^{\omega} d\omega' \, \alpha^2F(\omega')/\omega'$. The momentum-resolved el-ph coupling strength[12] $\lambda_{\boldsymbol{k}} = \Sigma_{\boldsymbol{k}',\nu} \, \delta(\varepsilon_{\boldsymbol{k}'})|g^{\nu}(\boldsymbol{k},\boldsymbol{k}+\boldsymbol{q})|^2/\omega_{\boldsymbol{k}-\boldsymbol{k}',\nu}$. The variation of el-ph coupling contributions across all electronic states within ±0.5 eV of the Fermi surface is shown by plotting the momentum-resolved el-ph coupling strength[12] (λ_k) in the Brillouin zone (Figure 5d). The momentum-resolved el-ph coupling strength (λ_k) in the Brillouin zone for electronic states only ±0.15 eV of the Fermi surface is shown in Figure S19(c). Lastly, T_c is given by the Mcmillan-Allen-Dynes formula $T_c = \omega_{\log}\exp[-\frac{1.04(1+\lambda)}{\lambda-\mu^*(1+0.62\lambda)}]$, where the logarithmic-averaged phonon frequency $\omega_{\log} = \exp[\frac{2}{\lambda}\int d\omega \log(\omega)\frac{\alpha^2F(\omega)}{\omega}]$ and μ^* is the coulomb pseudopotential. Finally, using the McMillian-Allen-Dynes formula[13,14] with λ=1.62 and μ^* in a range of 0.1 – 0.15 yields a T_c of 3.5 – 4.1 K, in agreement with the experimental measurements, compared to λ = 0.97 and T_c = 5.9 K for β-Ga[15] and λ = 0.40 and T_c = 1.08 for α-Ga[13].

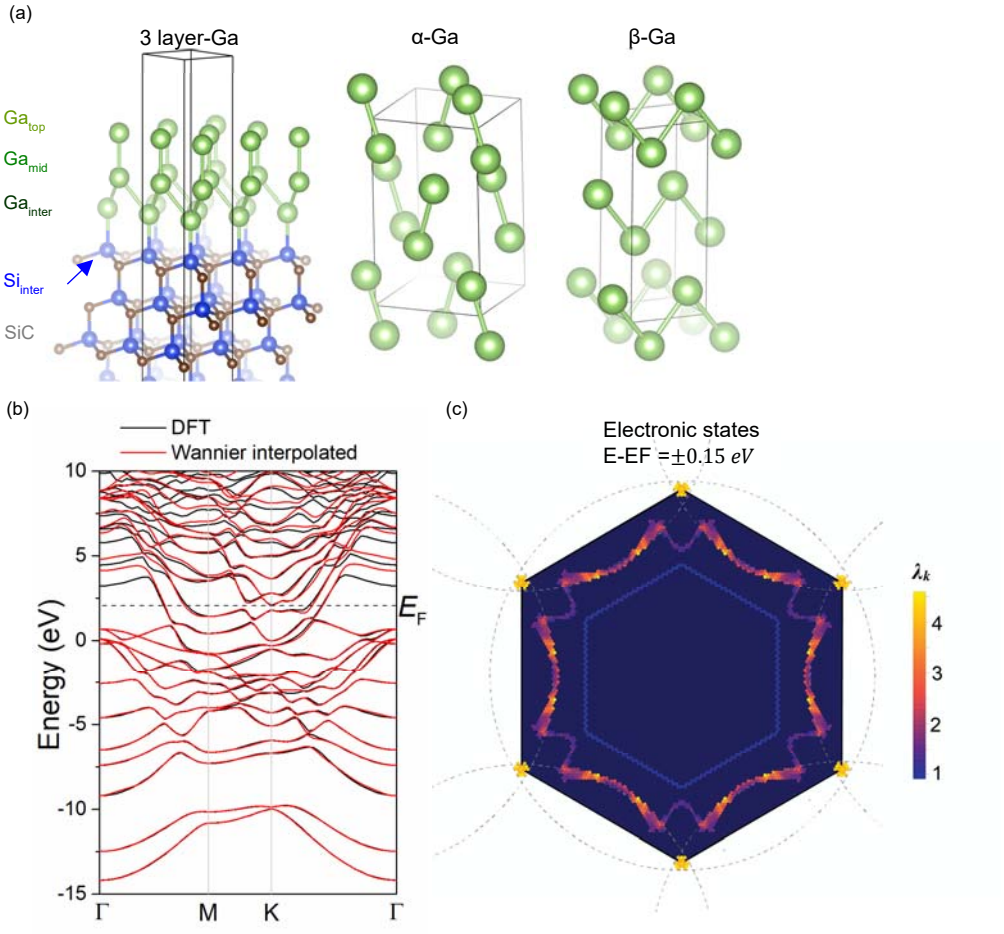

Figure S19: Theoretical calculations on graphene/2D-Ga heterostructures. (a) Atomic structure models of 3 layer Ga/SiC, α-Ga, and β-Ga phases used for DFT modeling. (b) Band structure of 3 layer Ga/SiC calculated from DFT (black) and from Wannier interpolation (red) based on the DFT Hamiltonian obtained on a regular 12×12×1 grid. A replication of DFT bands is only required within 0.5 eV of the Fermi level to ensure an accurate estimate of T_c. (c) Momentum-resolved electron-phonon coupling λ_k map for states within ± 150 meV from the Fermi level.

Decomposition of λ_k by phonon wavevectors

That the pockets are the main contributor to the electron-phonon coupling is already evident in the momentum-resolved el-ph coupling λ_k in Fig. S19(c), where electron pockets at K have the highest λ_k. Since λ_k contains the electron-phonon coupling for each k summed over all phonon wavevectors q, we further break $\lambda_{k=K}$ down into its q-dependent contributions $\lambda_{k=K,q}$ to identify which electron-phonon coupling matrix elements with initial states at K contributes most. The strongest contributions arise from intervalley scattering between the two K valleys (Figure S20 orange arrow), further demonstrating the importance of the electron pockets. As shown in Figure S21, the electron pocket states are mainly delocalized over the topmost Ga layer, consistent with the dominant phonons involved in $\lambda_{k=K,q}$ to be mostly vibrations of the topmost Ga atoms. Remarkably, 2D Ga is essentially a doped superconducting semiconductor overlaid with a nearly free electron metal.

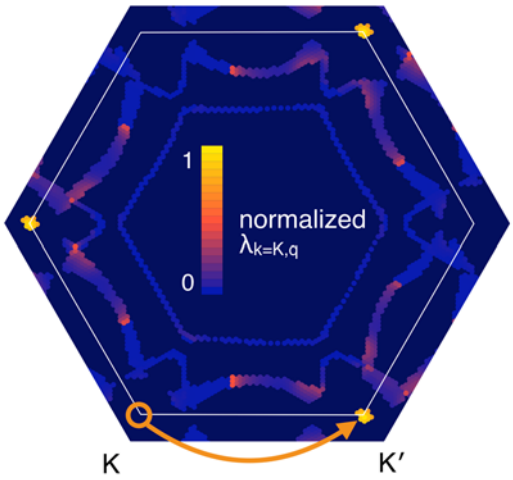

Figure S20: Momentum-transfer (q) resolved electron-phonon coupling matrix elements for the initial state at k=K. All final states at $K+q$ within ±0.15 eV of the Fermi surface are included. The highest contribution is from intervalley scattering (orange arrow).

Orbital characters of states near the Fermi surface

The above analysis of the Ga trilayer demonstrates the importance of the electron pockets contributed by the top-layer Ga. The other possible structure discussed in the main text (that would be consistent with ARPES if a Fermi level shift is allowed) is bilayer Ga on SiC. This is not computationally investigated here, since the appropriate electron-phonon coupling calculations in the bilayer system would require either manipulating electron occupancies (if the PBE exchange-correlation functional is used) or using the computationally much more expensive HSE hybrid functional for electronic structure and phonon calculations. In the bilayer Ga case, the electronic states that contribute most to λ are expected to be hole pockets at K (left panel of Figure S21, c.f. ARPES measurement in Figure 3b), with orbital character on both layers of Ga. Although an electronic state with similar orbital character in trilayer Ga exists, it resides too far above the Fermi level (~0.4 eV) to be included in the λ calculations, otherwise the electron-phonon coupling involving this state could inform the electron-phonon coupling in the bilayer Ga case.

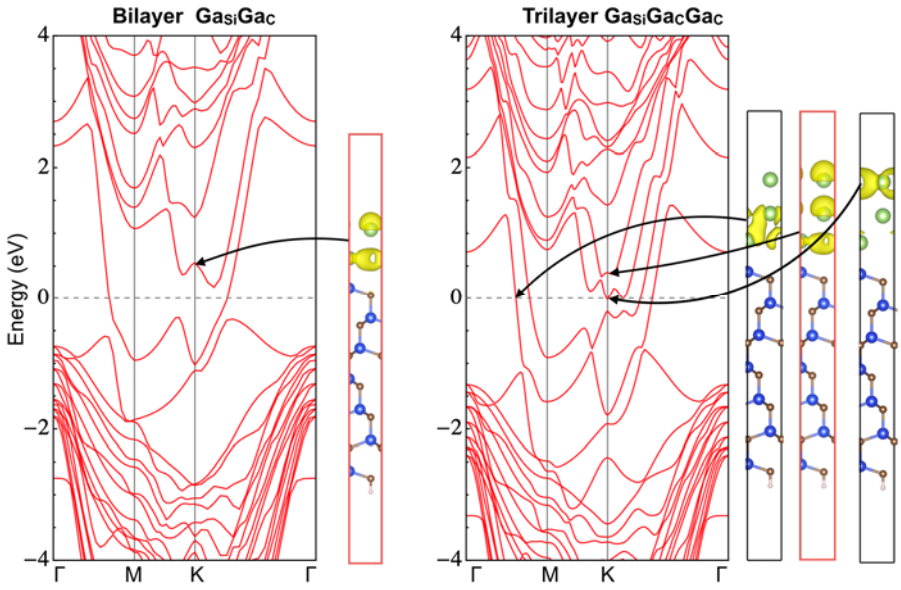

Figure S21: Orbital characters of states near the Fermi surface for (left) bilayer and (right) trilayer Ga.

Electronic structure for 1 layer Ga

The calculated band structure and DOS of 1 layer-Ga/SiC in Figure S22 shows more details on the presence of a gap around the Fermi energy.

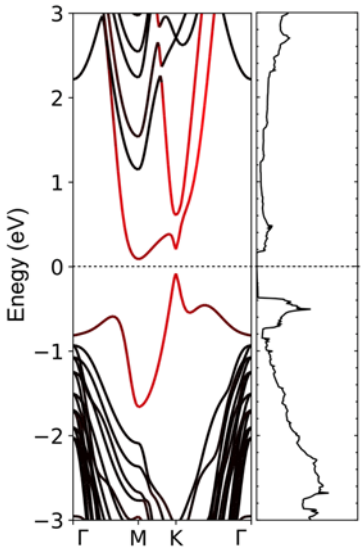

Figure S22: Band structure and DOS for 1 layer-Ga on 6H-SiC.

References

1. Zhang, T. *et al.* Superconductivity in one-atomic-layer metal films grown on Si(111). *Nat. Phys.* **6**, 104–108 (2010).
2. Uchihashi, T. Two-dimensional superconductors with atomic-scale thickness. *Supercond. Sci. Technol.* **30**, (2017).
3. Falson, J. *et al.* Type-II Ising Pairing in Few-Layer Stanene. *arXiv:1903.07627* (2019).
4. Noffsinger, J. & Cohen, M. L. Superconductivity in monolayer Pb on Si(111) from first principles. *Solid State Commun.* **151**, 421–424 (2011).
5. Choi, W. H., Koh, H., Rotenberg, E. & Yeom, H. W. Electronic structure of dense Pb overlayers on Si(111) investigated using angle-resolved photoemission. *Phys. Rev. B* **75**, (2007).
6. Choi, S.-M., Jhi, S.-H. & Son, Y.-W. Effects of strain on electronic properties of graphene. *Phys. Rev. B* **81**, 081407 (2010).
7. Riedl, C., Coletti, C., Iwasaki, T., Zakharov, A. A. & Starke, U. Quasi-Free-Standing Epitaxial Graphene on SiC Obtained by Hydrogen Intercalation. *Phys. Rev. Lett.* **103**, 246804 (2009).
8. Skocpol, W. J. & Tinkham, M. Ginzburg-Landau theory for superconductors. *Reports Prog. Phys.* **36**, (1973).
9. Reyren, N. *et al.* Superconducting interfaces between insulating oxides. *Science* **317**, 1196–9 (2007).
10. Zhang, H.-M. *et al.* Detection of a Superconducting Phase in a Two-Atom Layer of Hexagonal Ga Film Grown on Semiconducting GaN(0001). *Phys. Rev. Lett.* **114**, 107003 (2015).
11. Giustino, F., Cohen, M. L. & Louie, S. G. Electron-phonon interaction using Wannier functions. *Phys. Rev. B* **76**, 165108 (2007).
12. Margine, E. R. & Giustino, F. Anisotropic Migdal-Eliashberg theory using Wannier functions. *Phys. Rev. B* **87**, 024505 (2013).
13. McMillan, W. L. Transition Temperature of Strong-Coupled Superconductors. *Phys. Rev.* **167**, 331–344 (1968).
14. Allen, P. B. & Dynes, R. C. Transition temperature of strong-coupled superconductors reanalyzed. *Phys. Rev. B* **12**, 905–922 (1975).
15. Garno, J. P. Simple high vacuum evaporation system with low-temperature substrate. *Rev. Sci. Instrum.* **49**, 1218–1220 (1978).
16. Subramanian, S. *et al.* Properties of synthetic epitaxial graphene/molybdenum disulfide lateral heterostructures. *Carbon N. Y.* **125**, 551–556 (2017).
17. Giannozzi, P. *et al.* QUANTUM ESPRESSO: a modular and open-source software project for quantum simulations of materials. *J. Phys. Condens. Matter* **21**, 395502 (2009).
18. Joubert, D. From ultrasoft pseudopotentials to the projector augmented-wave method. *Phys. Rev. B* **59**, 1758–1775 (1999).
19. Blöchl, P. E. Projector augmented-wave method. *Phys. Rev. B* **50**, 17953–17979 (1994).
20. Perdew, J. P., Burke, K. & Ernzerhof, M. Generalized Gradient Approximation Made Simple. *Phys. Rev. Lett.* **77**, 3865–3868 (1996).
21. Perdew, J. P., Burke, K. & Ernzerhof, M. Erratum: Generalized gradient approximation made simple. *Phys. Rev. Lett.* **78**, 1396 (1997).
22. Marzari, N., Vanderbilt, D., De Vita, A. & Payne, M. C. Thermal Contraction and

Disordering of the Al(110) Surface. *Phys. Rev. Lett.* **82**, 3296–3299 (1999).
23. Stukowski, A. Visualization and analysis of atomistic simulation data with OVITO–the Open Visualization Tool. *Model. Simul. Mater. Sci. Eng.* **18**, 015012 (2010).
24. Momma, K., Izumi, F. & IUCr. *VESTA 3* for three-dimensional visualization of crystal, volumetric and morphology data. *J. Appl. Crystallogr.* **44**, 1272–1276 (2011).
25. Makov, G. & Payne, M. C. Periodic boundary conditions in ab initio calculations. *Phys. Rev. B* **51**, 4014–4022 (1995).
26. Neugebauer, J. & Scheffler, M. Adsorbate-substrate and adsorbate-adsorbate interactions of Na and K adlayers on Al(111). *Phys. Rev. B* **46**, 16067–16080 (1992).
27. Enkovaara, J. *et al.* Electronic structure calculations with GPAW: a real-space implementation of the projector augmented-wave method. *J. Phys. Condens. Matter* **22**, 253202 (2010).
28. Kresse, G. & Furthmu, J. Efficient iterative schemes for ab initio total-energy calculations using a plane-wave basis set. *Phys. Rev. B* **54**, 11169–11186 (1996).
29. Heyd, J., Scuseria, G. E. & Ernzerhof, M. Hybrid functionals based on a screened Coulomb potential. *J. Chem. Phys.* **118**, 8207–8215 (2003).